Prediction of Subject-specific Hip Cartilage Stresses Using Combined Musculoskeletal and Finite Element Modelling

Moa Johansson

Lund, June 2026

Master's Thesis in Biomedical Engineering

Faculty of Engineering LTH
Department of Biomedical Engineering
Main Supervisor: Lorenzo Grassi
Co-supervisors: Sana Jahangir & Daniel Benoit

Acknowledgements

I would like to start with a big thank you to all my supervisors who contributed to this thesis project. I am sincerely grateful to Lorenzo Grassi for his invaluable feedback and willingness to answer my numerous questions, helping to guide the thesis in the right direction. I would also like to thank Sana Jahangir for showing great interest in my work, share her expertise in FE modelling and provide valuable support throughout this thesis. Furthermore, I am grateful to Daniel Benoit for his valuable insights and advice in musculoskeletal modelling. Thank you all for dedicating your time, knowledge and effort to my master's thesis.

Finally, I would like to express my sincere gratitude to the entire division of biomechanics for always making me feel welcome and included in the group from the very beginning with a family-like atmosphere throughout my time there.

Abstract

Osteoarthritis is a degenerative joint disorder, which gradually breaks down cartilage and underlying bone. The disorder is commonly present in the hip joint, where it can cause anatomical changes that may result in painful movement. Early identification of osteoarthritis may facilitate treatment for slowing the disease progression.

This master's thesis aimed to develop a pipeline for applying subject-specific boundary conditions from motion capture data on a FE model of the hip joint. The pipeline combines experimental motion capture data, musculoskeletal modelling and finite element modelling into an integrated framework. Thus, prediction of cartilage stress distributions within the hip could be computed, providing insight into subject-specific alterations in cartilage loading that are thought to contribute to the initiation and progression of osteoarthritis.

Motion capture data from walking and running trials were used to extract hip kinematics and joint reaction forces for one single subject through musculoskeletal modelling. These outputs were used as inputs in the FE model to mimic subject-specific loading for simulations of the stance phase for walking and running, respectively.

Results showed that the computed joint reaction forces in the musculoskeletal modelling exhibited force profiles similar to those reported in literature with magnitudes of 4 body weight (BW) for walking and 8-9 BW for running. The predicted cartilage stresses exhibited similar ranges in magnitude compared to literature for both gaits with highest magnitudes of 11 MPa for walking and 13.5 MPa for running.

This pipeline provides a foundation for future studies to combine motion capture data into cartilage-level stress distributions through an integrated modelling framework. Thus, improved knowledge of stress distributions within healthy hips is enabled, which might support research for early detection and treatment of osteoarthritis.

Contents

1 Introduction

Osteoarthritis is a complex and painful disease, which progresses over time. It is a degenerative joint disorder characterized by gradual breakdown of cartilage and underlying bone. The prevalence of the disease is expected to increase due to an aging population [1]. An estimation made in 2019 showed that approximately 528 million people worldwide were affected by osteoarthritis [2]. Among the common joint sites, the disease is present in the hip joint. Since the middle-aged population is particularly affected by the disease, it poses a substantial economic and societal burden through lost workforce and early retirement [1]. Osteoarthritis can lead to anatomical changes in the joints, which may cause painful movement and loss of joint function. Consequently, the quality of life could be significantly reduced. Current treatment strategies include exercise therapy, lifestyle modification, pharmacological pain management and, in advanced stages, joint replacement surgery. The existing drugs might reduce the symptoms but are generally moderately effective and can cause side-effects during long-term use. Early identification of individuals at risk may facilitate interventions aimed at slowing the disease progression [1], [2].

In daily life, the hip joint experiences high magnitudes of load. The magnitude depends on the movement performed and the loads generated by the surrounding muscles, which ensure maintenance of balance. Hip joint contact forces can range approximately from a half body weight during perfect balance at two-legged stance to three times the body weight during single leg stance [3]. Previous studies have demonstrated that osteoarthritis may be associated with high contact pressures and shear stresses over time in the acetabular and femoral cartilage, particularly in dysplasic hips. Subject-specific methods for evaluating hip joint mechanics may therefore contribute to earlier identification of osteoarthritis and treatment. Furthermore, contact stress prediction may improve the understanding of cartilage mechanics in normal and pathological joints [4], [5].

Musculoskeletal modelling allows non-invasive estimation of physiologically realistic joint reaction loads within the hip by analysing gait. This is achieved by integrating subject-specific whole-body motion capture data with linked rigid-segment models, which replicate the structure of the human body [6], [7]. However, musculoskeletal modelling typically relies on simplified joint representations and lacks interpretation of the effect of the produced loads at a tissue level [8].

Finite element modelling enables non-invasive estimation of load distribution and provides insight into cartilage mechanics at a tissue level within the hip joint [4], [5], [9]. However, the accuracy of the analysis depends, among other things, on physiologically realistic loading input data, which is frequently simplified and may limit its ability to fully replicate real life mechanics [6], [10].

Musculoskeletal and finite element (FE) modelling have individually demonstrated potential for evaluating hip joint mechanics. By combining the two techniques, tissue level load distribution could be predicted based on physiologically realistic motion capture data [6], [11]. However, the combined approaches are still limited in research with few participants due to computational complexity [11]. These approaches have the potential to improve osteoarthritis prediction through enhanced understanding of cartilage mechanics in normal and pathological hip joints, thereby supporting earlier detection and treatment. Developing efficient subject-specific workflows that combine physiologically realistic motion capture data with detailed tissue level load analyses remains an important step toward clinically applicable biomechanical assessment tools.

1.1 Aim

The aim of this master's thesis was to develop a pipeline for applying subject-specific boundary conditions from motion capture data on a FE model of the hip joint. To address this aim, the work was divided into two main parts: a musculoskeletal model and a FE hip joint model with subject-specific loading. The musculoskeletal model part will extract the joint contact loads occurring within the hip joint from the motion capture data. The FE modelling of the hip joint include ilium, femur and the articular cartilage, and their material properties. The FE model is then connected to the musculoskeletal model by using its predicted joint contact forces as boundary conditions for the FE simulation to compute cartilage stress distributions within the hip.

1.2 Structure of this report

An overview illustration of the structure of this report is visualized in Figure 1.1. The report is divided into a musculoskeletal modelling section and a finite element modelling section with subject-specific loading, which are further integrated into a combined approach. Based on experimental data, inverse kinematics analysis of a musculoskeletal model was initially performed to estimate subject-specific joint kinematics. This was followed by static optimization and joint reaction analysis to determine the joint reaction forces acting across the hip joint. A subject-specific finite element model was developed, incorporating material properties, interactions and a cartilage contact definition to reproduce hip joint mechanics. The two approaches were combined to implement the computed joint reaction forces and rotations into the finite element model with subject-specific loading, thereby replicating the experimental movements and enable evaluation of the cartilage stress distributions within the hip joint.

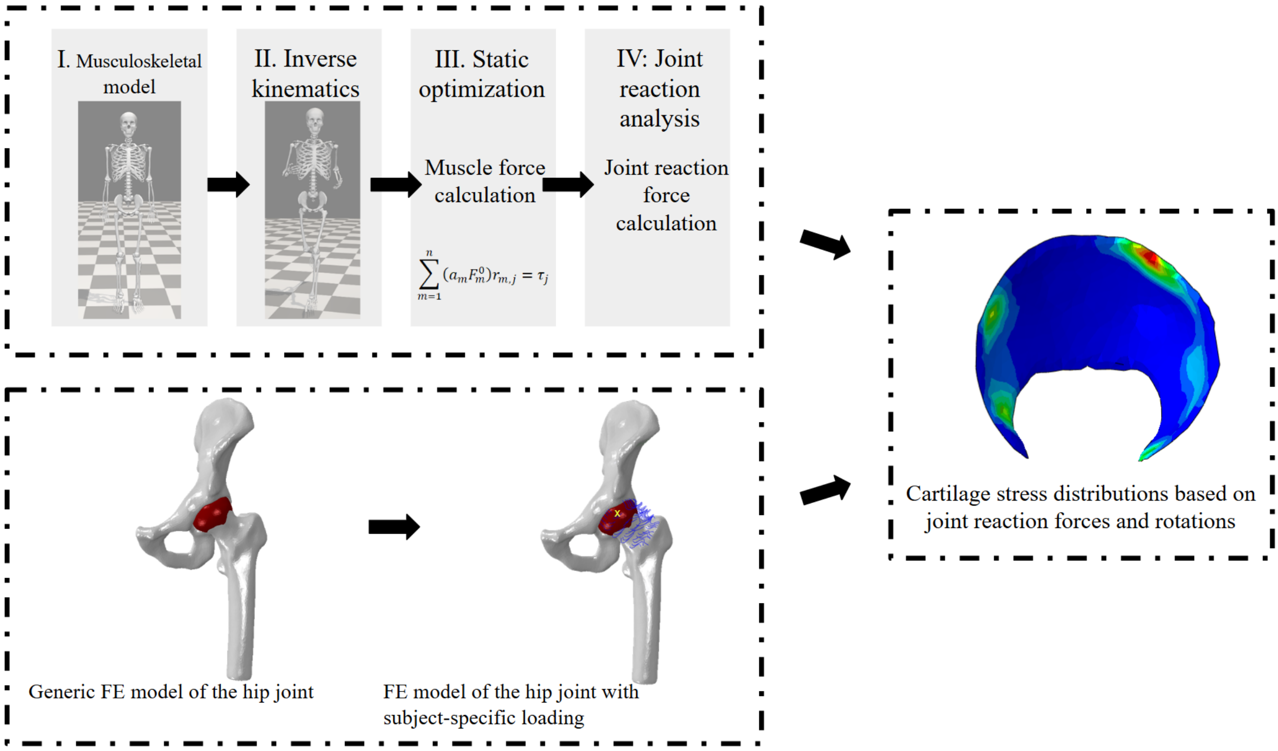

Figure 1.1: A schematic illustration of the structure of this master's thesis.

2 Background

The following section outlines the theoretical background behind this master's thesis, including anatomy and biomechanics of a hip joint along with the progression of osteoarthritis. Relevant theory for musculoskeletal and finite element modelling with subject-specific loading is also described in this section.

2.1 Hip Anatomy

2.1.1 Bone

The hip joint is a ball-and-socket joint embedded within muscles, providing stability and an extensive variability across various physical planes [12], [13]. It serves as a weight-bearing and load-transmitting interface by distributing forces from the head, neck, trunk and upper extremities, while also transmitting forces from the ground. Thus, the hip joint plays a central role during athletic activities, where it is exerted to numerous greater than normal axial and torsional forces [12].

The hip joint consists of the femoral head, the acetabulum of the pelvis and the articular cartilage (Figure 2.1). The pelvis is composed of two hip bones connected anteriorly at the pubic symphysis. The pubis, ischium and ilium form each hip bone [13], [14]. On each side, the hip bone connects with the sacrum, forming the sacroiliac joint [14]. The femur is the longest and strongest bone in the human body with weight-bearing properties and provide gait stability. Two bony protrusions, the greater and lesser trochanter, are located on the femur. They serve as attachment points for muscles, enabling hip and knee movement [15]. The femoral head articulates with the acetabulum, a cup-shaped cavity located in the pelvis [16].

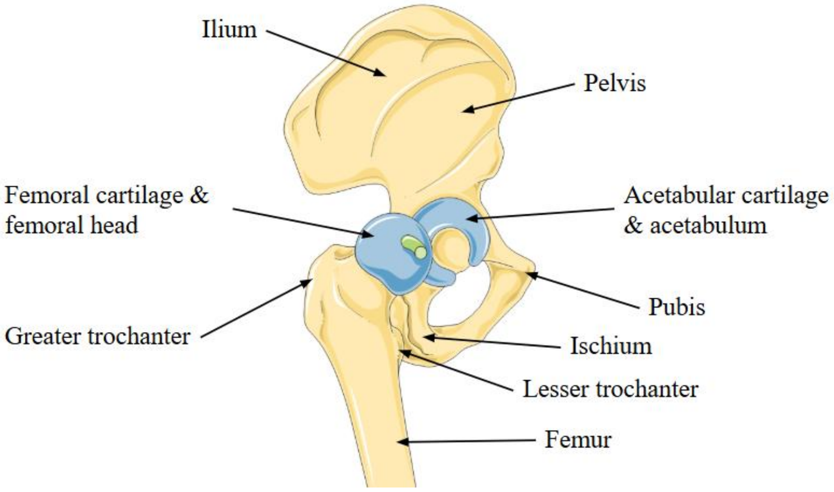

Figure 2.1: An illustration of the hip joint including the pelvis, femur and the articular cartilage. Adapted from [17].

Bone is a complex anisotropic, nonlinear and hierarchical material. Its mechanical properties correlate to geometry, density, microstructure and material properties [18]. The main function of bone is to provide structural support and facilitate movement. The muscles anchor to bones, mimicking a lever system for movement and thereby enabling body movement [19]. At a macro scale, bone exhibits a linear elastic behaviour between stress and strain at low strains with similar elastic parameters for tensile and compressive loads [18]. Bone could be categorized into two types: cortical bone and trabecular bone. Cortical bone is dense with a hard outer layer and provides support, strength and protection [19]. It is crucial for resisting compression and bending forces [18], [19]. In contrast, trabecular bone is less dense and is located at the interior regions of long bones and within vertebrae [19].

In FE analysis bone is often modelled as an isotropic elastic material [4], [5], [20], [21], [22]. An isotropic material exhibits similar mechanical and physical properties in all directions. The main parameters used to characterize this material are Youngs's modulus (E) and Poisson's ratio (ν) [20].

2.1.2 Cartilage

Cartilage exists in different forms and enables various functions in the human body, depending on its composition. In joints, its primary function is to serve as a binder or to bear the surface between bone ends. In synovial joints, i.e. the hip joint, the articular cartilage acts as a bearing surface, allowing for smooth motion between adjacent bone ends. In these joints, the bone ends are covered with articular cartilage, enabling a bearing surface with a relatively low friction coefficient (~0.001), while allowing load distribution between the bone ends in the joint [23]. In the hip joint, both the femoral head and acetabulum are covered in articular cartilage. The cartilage on the femoral head extends beyond the edges of the acetabulum, which contributes to the hip's full range of motion [12], [13]. In contrast, the acetabular cartilage is C-shaped and does not cover the whole acetabulum [16].

The main component of cartilage is water, which constitutes approximately 70 % to 85 % of the whole tissue. The remaining part is predominantly composed of collagen and proteoglycans, where collagen constitutes approximately 60 % to 70 % of cartilage's dry weight. Together with the water content, these components form the ECM [23], [24]. The articular cartilage is often categorized into four zones that extend between the articular surface and the subchondral bone: the superficial area, the middle area, the deeper area and the calcified area [23], [24]. In the superficial zone the collagen fibers are parallel aligned to the articular surface and form a compact fibrous structure. This zone exhibits the primary tensile properties of cartilage and thereby resists shear, tensile and compressive forces. In the middle zone, about 40 % to 60 % of the tissue, the collagen fibers in obliquely structured. In the deep zone, the collagen fibrils are perpendicular aligned to the articular surface and withstand the majority of the compressive forces [24].

The articular cartilage can be modelled biphasic divided into a solid and a fluid phase [23], [24]. The primary component of the fluid phase is water, while the solid phase encompasses the ECM. The interstitial fluid pressure immediately increases with an initial and rapid load on the joint, causing articular contact forces. Thus, the fluid flows out of the ECM and produces a large frictional drag on the matrix [24]. However, during impact loads the cartilage exhibits a single-phase, incompressible, elastic behaviour due to the insufficient time preventing the fluid to flow out of the ECM [23].

Cartilage exhibits a time-dependent and nonlinear behaviour in tension and compression. It could therefore be difficult to determine which material model that is most suitable to use. The choice depends on the loading scenario considered, its complexity and which mechanical behaviour is aimed to be captured. Commonly, the chosen material model is a simplest one that adequately represents the behaviour relevant for the research question [25]. Despite the biphasic behaviour of cartilage, a equivalence has been demonstrated in computational stress predictions between a biphasic and an incompressible hyperelastic material model during instantaneous loading [4], [5]. Hence, a neo-Hookean hyperelastic material is often used to describe cartilage in FE analysis

[4], [5], [6], [25], [26], [27]. Initially, for smaller strains, a hyperelastic material exhibits an elastic stress-strain response, while the response becomes non-linear for larger strains [28]. The hyperelastic response is path independent and reversible, where the response for loading and unloading follows the same path. The hyperelastic material returns to its initial configuration after removing the load. Its behaviour could be described by the following relationship between stress σ, strain energy W and strain ε:

$$\sigma = \frac{\partial W}{\partial \varepsilon} \tag{2.1}$$

where the stress is derived from the strain energy, that is the energy stored in a material per unit of its original configuration [29], [30], [31]. Generally, the strain energy W depends on the current strains ε and in which way the strains are gained, which could be described as follows:

$$W = W(\varepsilon, \text{load history}) \tag{2.2}$$

However, the current stresses σ only depend on the current strains ε [29].

A neo-Hookean hyperelastic material model used for modelling cartilage is described by a shear modulus μ and a bulk modulus K [28]. It is characterized by the following equation:

$$U = C_{10}(\bar{I}_1 - 3) + \left(\frac{1}{D_1}\right)(J^{e\ell} - 1)^2 \tag{2.3}$$

In Equation (2.3), the variable U refers to the strain energy per unit of the reference volume, C_{10} and D_1 correspond to temperature-dependent material parameters, $\bar{I}_1$ is the first deviatoric strain invariant and $J^{e\ell}$ refers to the elastic volume ratio [32].

2.1.3 Ligaments

The hip joint capsular ligaments are crucial for balancing joint stability and functional mobility. They wrap around the acetabulum periosteum and proximal femur, holding the femoral head within the acetabulum [15], [33]. Together, they restrain internal rotation, while allowing complex combinations of planar movements and rotation [15], [34].

The hip capsule is primarily composed of the iliofemoral, ischiofemoral, pubofemoral and the teres ligament, see Figure 2.2. The iliofemoral ligament is divided into a superior and inferior branch. The branches support the ligament during external rotation and extension. Both branches insert into the anterior inferior iliac spine of the pelvis and attach along the femoral intertrochanteric line. The ligament also provides a static constraint to full hip extension, enabling maintenance of an erected posture without constant muscular action. The ischiofemoral ligament extends from the ischial rim of the acetabulum to the posterior intertrochanteric line. Thus, it supports the hip capsule during rotation in neutral positions and combined flexion-adduction rotations. The pubofemoral ligament is inserted into the superior pubic ramus and merge with the medial iliofemoral and inferior ischiofemoral ligaments to attach to the femur. Thus, it supports the inferior capsule to restrain excessive abduction and external rotation during hip extension. The teres ligament couples the peripheral inferior acetabular notch to the fovea of the femoral head, providing structural stability [33], [34] .

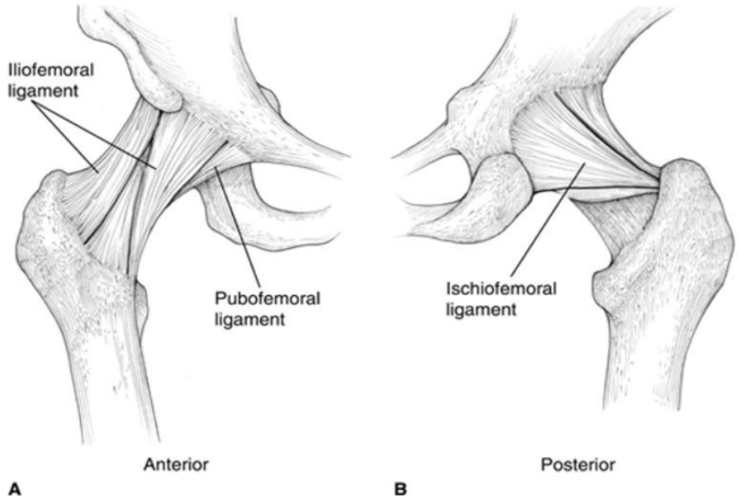

Figure 2.2: An illustration of the hip capsule composed of ligaments from A) an anterior perspective and B) a posterior perspective. Adapted from [13].

2.1.4 Muscles

The human body is composed of three muscle types: skeletal, cardiac and smooth. The skeletal muscles connect muscles to bones and provide strength. Its muscle contractions permit specific movements, maintain posture, store amino acids, provide structural support and support temperature regulation via shivering. The muscle fibers are divided into two groups: striated and smooth muscle fibers. Skeletal muscle tissue contains striated muscle fibers, which control contraction via voluntary control. Interiorly, striated muscle fibers contain smaller entities called myofibrils. These entities consist of parallel thin (actin) and thick (myosin) filaments, which in turn are longitudinally organized in small entities called sarcomeres [35].

The muscle contribution in any movement or contraction is complex, particularly in highly skilled movements where many muscles are involved [36]. Muscles are redundant, meaning multiple combinations of muscles can produce the same coordinated movement. Thus, it is not trivial to compute individual muscle forces and activations [8]. It could therefore be challenging to distinguish the selection and the actual number of muscles involved in a movement [36]. It has been shown that the greatest muscle contributions during running is performed by gluteus maximus, gastrocnemius, soleus, hamstrings and the vastus muscles [37], [38], [39]. Since this master's thesis focus on the hip joint, only the gluteus maximus and the hamstrings are relevant.

During running, gluteus maximus predominantly decelerates the swing-leg, extends the thigh and controls flexion of the trunk on the stance-side and flexion of the hip. Near the footstrike, its peak activity is achieved. In comparison to walking, the gluteus maximus is significantly more active during running [40].

The hamstrings are central in numerous daily life movements, including walking and running. Together with gluteus maximus, the hamstrings produce an eccentric action to decelerate the rate of hip flexion during the final swing phase in gait, respectively generating a concentrical action during hip extension. The hamstrings are particularly essential in sport activities including jumps, kicking and sprints [41].

Muscle forces are practically unmeasurable to directly obtain from human muscles during voluntary contraction. Thus, the knowledge of muscle force and its mechanics is derived from musculoskeletal model estimations. Muscle force estimations are an indeterminate problem; the number of muscles is greater than the degrees of freedom in the human body. Movement patterns have been analysed using musculoskeletal models. However, musculoskeletal models exhibit a great number of dimensions and high architectural complexity. To investigate the effects from muscle forces within joints, these forces can be incorporated as loading conditions in numerical methods, i.e. finite element method (FEM), which is solved using approximations. By using a combination of musculoskeletal models and FEM, it is possible to obtain muscle models of greater complexity in simulations of whole-body movement [42].

2.2 Biomechanics of the Hip Joint

Hip joint biomechanics arise from the interaction between body weight, muscle forces and joint reaction forces that together enable balance and movement. A combination of translations and rotations in x, y and z direction characterize joint motion, which include 6 degrees of freedom. Since the hip joint is a ball-and-socket joint, it exhibits 6 degrees of freedom. In daily activities, including walking, the hip joint can resist all stresses exerted upon it and its range of motion is greater than needed in the daily life. Muscle forces are crucial in hip stability during gait. i.e. walking and running [13].

Static equilibrium conditions, indicating motionless movement or movement at constant acceleration, are not fulfilled in gait due to movement of body parts and change of direction, i.e. acceleration [43]. The generated forces during movement can be formulated by Newton's second law where the force F is expressed as following:

$$\sum F_{x,y,z} = \mathrm{m} \times \mathrm{a} \tag{2.4}$$

In Equation (2.4), m refers to mass and a corresponds to acceleration. The corresponding rotational relationship regarding the produced moments M can be expressed as following:

$$\sum M_{x,y,z} = I \times \alpha \tag{2.5}$$

In Equation (2.5), I refers to inertia and α corresponds to angular acceleration. During stance phase, the body is temporarily standing on a single limb, which is illustrated in Figure 2.3. The force from the body weight (BW) acts downwards, generating a rotatory motion around the femoral head. This motion is created by the body weight and the moment arm between the femur and the centre of gravity. Thus, it pulls the body to lean over, which is counterbalanced by the combined action of the abductor muscles [3], [13]. Hence, the hip could be mimicked as a lever with a load exerted on either side of the femoral head [3].

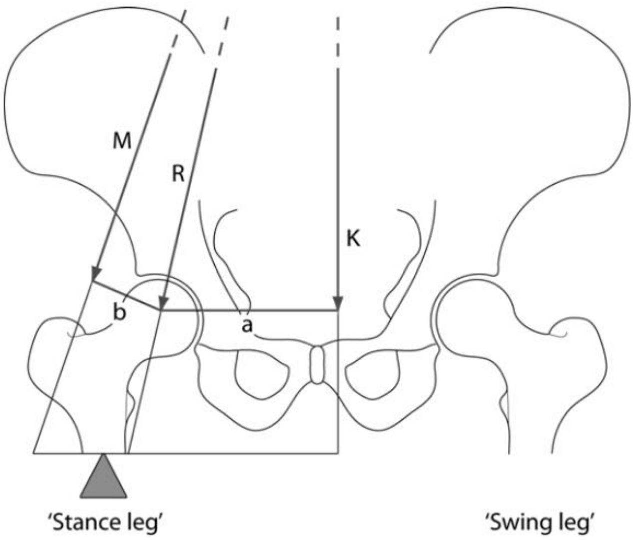

Figure 2.3: A free body diagram illustrating the computation of hip joint force during gait. M corresponds to the abductor muscle force, R refers to the joint reaction force and the body weight minus the weight bearing leg is represented by K. The moments arms are expressed as a and b. Adapted from [12].

In contrast to gait, both hips carry the body weight in a standing position. The magnitude of joint reaction forces can range approximately from 1/2 BW (perfect balance during two-legged stance) to 3BW (single leg stance). Thereby, the abductor muscles are essential to maintain balance and pelvic stability. Consequently, their function becomes of greater importance in dynamic motions. Even when no body weight is applied, the hip is never fully unloaded. The abductor muscles continuously control the leg during swing phase. However, the magnitude of movement generated by the abductor muscles is much smaller during swing phase compared to stance. Therefore, significant changes in hip mechanics require compensatory strategies from the patient to maintain balance and equilibrium. Hip pain due to osteoarthritis could be decreased by reducing the joint reaction force [3].

2.3 Osteoarthritis

Osteoarthritis is a painful and complex disease that affects millions of individuals worldwide. The hip is among the common joints involved, where the risk of developing osteoarthritis increases with age, obesity, inheritance and prior joint trauma. In severe cases, the disease can cause radiological changes, including joint space narrowing, subchondral bone sclerosis and formation of osteophytes. These changes could result in pain, stiffness and loss of joint function. Osteoarthritis is the most common reason for total hip replacement. However, symptom severity varies over time, between individuals and across joint sites.

The high prevalence of the disease in middle-aged individuals poses a significant burden through lost working capacity and early retirement. Although the prevalence is difficult to determine, it is expected to increase due to the aging population [1].

Improved knowledge of load distribution in normal and pathological joints could be obtained by predicting contact stresses within the hip joint. Studies has demonstrated that high contact pressures and shear stresses over time in the acetabular and femoral cartilage of dysplasia hips may be associated with osteoarthritis. Subject-specific methods for evaluating hip mechanics may help predict osteoarthritis and thereby enable early diagnosis and treatment [4], [5].

2.4 Musculoskeletal modelling

Quantification of biomechanical factors, that are usually unmeasurable, could be obtained by using musculoskeletal modelling, i.e. hip contact forces and moments. Musculoskeletal modelling can be used to identify potential causes associated with pathological movements. Thus, the outcome could establish an evidence-based foundation to find the optimal treatment for individuals [44]. These models are commonly used in studies to evaluate both healthy and pathological populations [6], [11], [45], [46].

Musculoskeletal models consist of motion capture data and linked rigid-body segments connected by joints to mimic the human body. The motion capture data contains marker data and ground reaction force data obtained from force plates in the floor or treadmill during the experimental trials [7]. Thereby, estimation of internal loading of musculoskeletal systems can be examined, i.e. muscle forces and loads within joints [8].

Joint load estimation is performed using a musculoskeletal model together with inverse kinematics data, external loads between the foot and the floor captured by motion data and a muscle force estimation [47]. Initially, the musculoskeletal model is scaled according to the anthropometry of the individual subject. Joint angles and translations are further determined by an inverse kinematics problem, by which the model markers are aligned to the experimental markers. The calculation is usually solved by a least-squares problem, which minimizes the difference between the measured marker location and the model's virtual location and is formulated as follows [8], [48]:

$$\min_{\boldsymbol{q}}\left[\sum_{i\in markers} w_i \left\|\mathbf{x}_i^{exp}-\mathbf{x}_i(\mathbf{q})\right\|^2+\sum_{j\in unexpected\ coords}\omega_j\left(q_j^{exp}-q_j\right)^2\right] \quad (2.6)$$

In Equation (2.6), $\mathbf{q}$ refers to the vector of generalized coordinates being solved for, $\mathbf{x}_i^{exp}$ is the experimental position of marker i, $\mathbf{x}_i(\mathbf{q})$ is the position of the corresponding model marker, q_j^{exp} is the experimental value for coordinate j and w_i is the marker weights respectively ω_j is the coordinate weights [48].

Estimation of muscle forces is an indeterminate problem: the number of unknowns (muscle forces) is greater than the number of constraints (equations) [7]. Thus, static optimization is required to calculate the muscle forces acting in the analysed movement [47]. The optimization utilizes the known motion to find solutions to equations of motions for the unknown forces. The expression for ideal force generators is given as follows:

$$\sum_{m=1}^{n}(a_m F_m^0) r_{m,j} = \tau_j \quad (2.7)$$

In Equation (2.7), n refers to the number of muscles in the model, a_m is the activation level of muscle *m* at a discrete time step, F_m^0 is the maximum isometric force, $r_{m,j}$ is the moment arm about the jth joint axis and τ_j is the force acting about the jth joint axis [49]. The outcome is one possible distribution of muscle forces to generate the measured joint kinematics. The combination of the musculoskeletal model with inverse kinematics, external forces and static optimization provides a complete description of the dynamics for a certain movement [47].

Furthermore, joint reaction loads could be estimated using the muscle force estimation obtained from the static optimization. Joint reaction analysis computes joint loads transferred between two adjacent body segments, i.e. the pelvis and the femur, thereby providing the resultant internal forces and moments acting across the joint. For the hip joint, the computed joint reaction forces correspond to the sum of contact forces across the joint, including contributions from the acetabular and femoral cartilage and ligament forces [50].

The internal loads, i.e. joint reaction loads, are not obtained directly when solving the equations of motion of the musculoskeletal model because of the formulatation of generalized coordinates and forces. Instead, joint reaction loads are computed in a post-processing step using muscle forces and joint kinematics. The calculations are performed iteratively starting at the most distal body segment and progressing proximally through the musculoskeletal model. At each joint, joint reaction forces are determined by balancing external and inertial forces acting on the distal body segment. This process involves constructing a free body diagram for each rigid body segment and solving for an unknown joint point load that is needed to balance the forces and motions of the body [50]. An illustration of the free body diagram is shown in Figure 2.4.

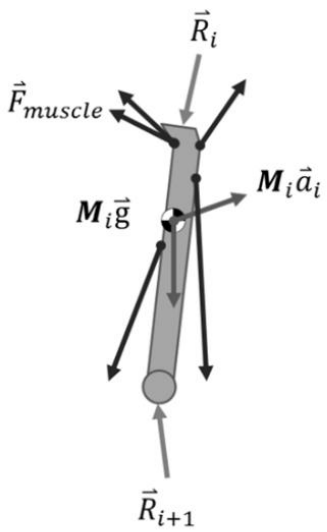

Figure 2.4: A free body diagram of a rigid body segment illustrating the computation of the proximal joint reaction load, $\vec{R_i}$, based on the body segment's inertial forces, muscle forces (shown as black arrows), other external forces and the previously determined joint reaction force at the distal joint, S_i. Adapted from [50].

For joint i, the resultant forces and moments at the joint, $\vec{R_i}$, were calculated by isolating the distal body segment, S_i, and treating it as an independent body with known kinematics in a global reference system. Joint kinematic complexity was captured through accelerations, $\vec{a_i}$, reconstructed from the generalized equations of motion [50]. The relationship between this and the calculated joint reaction force and moment could be expressed as follows:

$$\overrightarrow{R_o} = \begin{bmatrix} \overrightarrow{\tau_o} \\ \overrightarrow{F_o} \end{bmatrix} = \boldsymbol{M}_i(\vec{q})\vec{a}_i + \vec{F}_{constraint} - \left(\sum \vec{F}_{external} + \sum \vec{F}_{muscle} + \vec{R}_{i+1}\right) \quad (2.8)$$

In Equation (2.8), the previously computed forces and moments applied by the external loads and musculotendon actuators are represented by $\vec{F}_{external}$ and $\vec{F}_{muscle}$ respectively. The $\vec{R}_{i+1}$ corresponds to the previously calculated load at the distal joint and constraint forces are represented by $\vec{F}_{constraint}$. This equation balances the inertial effects of each body segment with external loads, constraint forces, muscle forces and loads transferred from the adjacent distal joint [50].

A combination of musculoskeletal and finite element (MS-FE) modelling enables more detailed studies of joint loading and mechanical responses at a tissue-level [11]. Commonly, the joint loads calculated from a musculoskeletal model serve as inputs to simulate contact mechanics in a FE model, i.e. a hip joint model[6]. However, the MS-FE models are yet limited to research applications with few participants due to the great time consumption and requirement of expertise, making them clinically unsuitable [11].

In this master's thesis, musculoskeletal modelling is used to estimate joint loads within the hip joint. This analysis is performed in OpenSim 4.5 [51], which provides an open-source software for modelling, simulation and analysis of a musculoskeletal model [8].

2.5 FE modelling

2.5.1 The Standard FE Formulation

Computational modelling is widely used in biomechanics. In hip mechanics, the method enables potential prediction of hip joint cartilage mechanics noninvasively, resulting in a deeper knowledge of load distribution in normal and pathologic joints. Numerous studies have used the finite element method as a tool to predict these load distributions within the hip joint [4], [5], [9].

In engineering mechanics, physical problems can be modelled by differential equations. This technique is used due to the complexity of solving problems using classical analytical methods. A numerical approach that is commonly used is the finite element method (FEM), which solves general differential equations using approximations. For example, the deformation of an axial loaded elastic bar can be described by the following one-dimensional equilibrium equation:

$$\frac{d}{dx}(AE\varepsilon) + b \ = 0 \tag{2.9}$$

, where A refers to the cross-sectional area, E is Young's modulus, b is the axial loading exerted on the bar and ε is the strain defined by $\frac{du}{dx}$ where $u(x)$ refers to the displacement. An assumption made in the finite element method entails that the differential equations describing the considered problem hold over a specific region. The region could be one-, two- or three-dimensional. Instead of solving approximations directly for the entire region, the considered region is divided into smaller entities, so called finite elements. Thus, approximations are solved for each element. This approach is relatively straightforward compared to a direct approximation over the entire region. The approximations express the determined behaviour of how variables (i.e. displacement) change over a specific element. By summing all approximations for each element, a FE mesh is created. Usage of specific rules enables the mesh to express the behaviour of the entire region. Thus, an approximated solution is obtained describing the behaviour of the entire region [10].

When solving a FE problem, the first step is to obtain a strong formulation, which characterizes the considered problem. The strong formulation is multiplied with a weight function v chosen according to Galerkin's method and integrated by parts using the Green-Gauss theorem. The expression is then rewritten into the weak formulation of the considered problem. A weak formulation of a one-dimensional mechanical problem could be expressed as follows:

$$\left(\int_a^b \boldsymbol{B}^T AE\boldsymbol{B}dx\right)\boldsymbol{a} = -[\boldsymbol{N}^T A\varepsilon]_a^b + \int_a^b \boldsymbol{N}^T bdx \tag{2.10}$$

In Equation (2.10), **B** refers to $\frac{dN}{dx}$, A is the cross-sectional area, **a** is the nodal displacements, E is the Young's modulus, ε is the strain, **N** is the shape functions and b is the loads acting on the region. From Equation (2.10), the global FE formulation is obtained:

$$\boldsymbol{Ka} = \boldsymbol{f} \tag{2.11}$$

, where **K** refers to the stiffness matrix, which is defined as $\int_a^b \boldsymbol{B}^T AE\boldsymbol{B}dx$. **a** is the displacement vector. **f** includes two vectors: the load vector ($\boldsymbol{f_l} = \int_a^b \boldsymbol{N}^T bdx$) and the boundary vector ($\boldsymbol{f_b} = -[\boldsymbol{N}^T A\varepsilon]_a^b$). The load vector refers to the effects of the loading, while the boundary vector contains the conditions at the boundary [10].

In this master's thesis, the standard FE formulation is computed in the FEA software Abaqus [52], which further offers analysis of the FE model of hip cartilage mechanics.

2.5.2 Finite Element Mesh and Element Type

A mesh of a FE model consists of finite elements, enclosing the geometry of the model [10]. In computational biomechanics, the most commonly used three-dimensional elements are hexahedral and tetrahedral elements, see Figure 2.5 [25]. Complex biological geometries are commonly meshed using 4-noded linear tetrahedral elements (C3D4) due to automatic tetrahedral mesh generators [25],

[53]. In a simple femur model, it has been demonstrated that usage of tetrahedral linear elements yields outcomes more consistent with theoretical results than hexahedral quadratic elements. However, hexahedral quadratic elements seemed more stable and less affected by the level of refinement of the mesh [53].

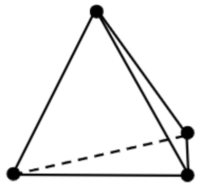

Figure 2.5: A four-noded tetrahedral element.

3 Materials & Method

This section presents the methodology used in this master's thesis separated into two subsections: The Musculoskeletal Model and The Finite Element Model.

3.1 The Musculoskeletal Model

This subsection presents the methodology used for the musculoskeletal modelling in this thesis. An overview of the conducted analyses is illustrated in Figure 3.1.

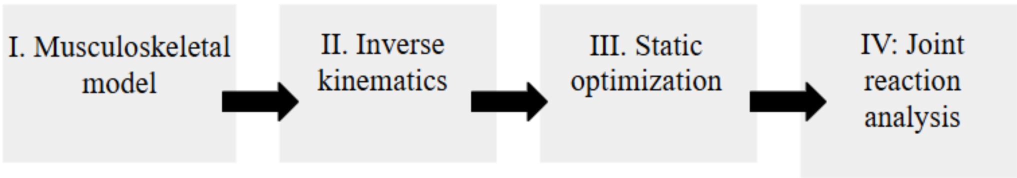

Figure 3.1: A schematic of the workflow in the musculoskeletal modelling.

3.1.1 The Experimental Data

Experimental data used in this master's thesis was available from MoRe-Lab in Lund. The data included a group of 23 athletes (13 males and 10 females) with a mean age of 24.26 +/- 4.02 years. Before the trials, anthropometric measurements were obtained for each subject including height, weight, leg length, tibial length, thigh circumference, shank circumference, ASIS and PSIS measurements. Surface electromyography (sEMG) electrodes were placed on the muscle bellies to record muscle activation. Additionally, the subjects were fitted with 56 reflective markers based on the Qualisys Sport Marker set and the convention described by Mantovani and Lamontagne (2017). Motion capture data were collected using a ten-camera 3D motion analysis system. Embedded force plates sampling at 1000 Hz recorded the corresponding kinetic data from the instrumented treadmill (HP Cosmos, Germany) with a capacitance-based pressure platform (FDM-THG, Zebris Medical GmbH, Germany) [54].

Each subject conducted a high-intensity running protocol at 85 % of VO2 max speed on a treadmill set to 1 % incline. The protocol had a maximal duration of 30 minutes. Before the trial, the subjects completed a warm-up of 3-minutes walking at 5 km/h and light jogging for 2.5 minutes at 8 km/h. During the 85 % VO2 max protocol, metabolic data, GRF, kinematics, pressure mat and EMG data were measured at 5-minute intervals for 30 seconds. Following the protocol, after the trial the subjects walked at 5 km/h followed by jogging for one minute at 8 km/h before being weighed [54].

The pipeline was developed using data from one of the available subjects. The measurements incorporated in the musculoskeletal modelling procedures for the analysed subject are shown in Table 3.1.

	Height	Weight	Running speed	Walking speed
Measurements	172.4 cm	66.6 kg	10.5 km/h	5 km/h

Table 3.1: The measurements used in this pipeline for the analysed subject.

3.1.2 Musculoskeletal Simulations

The musculoskeletal model used was a so-called Catelli model [55], which was beforehand scaled according to the anthropometry of the subject, see Figure 3.2.

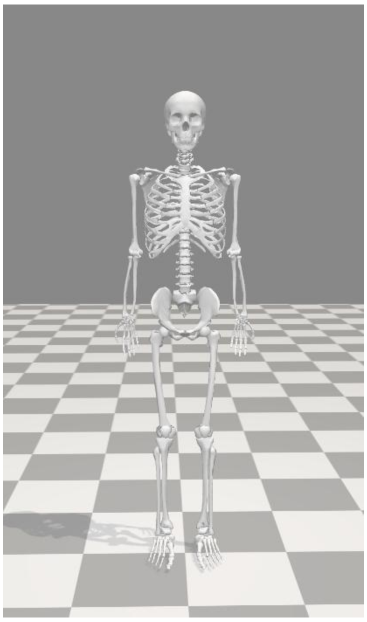

Figure 3.2: The Catelli model used and scaled according to the anthropometry of the subject is visualized in a static position.

The musculoskeletal simulations were performed in OpenSim. All simulations were computed for both walking and running. An inverse kinematics analysis was computed to obtain joint angles and translation based on the experimental data. The model used contained 56 markers corresponding to the reflective markers attached to the subject during the experimental data. The markers were weighted according to the muscle contributions in the experimental data with greater weighting to the markers located at the left and right anterior waist and the left and right superior iliac posterior. The time range used included the full time of the experimental data. The inverse kinematics analysis aligned the subject's makers with the virtual model's markers by calculating a weighted least squares problem.

Muscle force estimation was calculated by static optimization. The computed inverse kinematics data was used as an input file for this analysis. The time range used was identical to the inverse kinematics. In the static optimization analysis, a cut-off frequency of 6 Hz was used to filter the coordinates in the input file to reduce high-frequency noise. The default settings for the step interval of 1, the sum of muscle activation to the power of 2 and precision of 8 were used. Ground reaction forces from the experimental data were used as external loads and actuators was available from MoRe-Lab in Lund [54].

Joint reaction analysis was further used to estimate hip joint reaction forces and moments based on the experimental data. An identical setup was used in this analysis as in the static optimization: the same inverse kinematics file served as input and identical step interval, time range, precision, actuators and external loads were used. Additionally, the option of filtering the coordinates at 6 Hz was activated. The muscle force estimation obtained in the static optimization step was used as force file in the joint reaction analysis. The analysis generated an output file containing all joint reaction loads acting within the joints of the musculoskeletal model during the execution of the experimental data, that is for walking and running respectively.

3.1.3 Extraction and Preprocessing of Joint Loads for FE Model Input

To implement the computed joint reaction loads, including forces and moments, for the hip joint, the output file of the joint reaction analysis required filtering to only obtain loads relevant for the hip joint. These loads underwent further preprocessing to enable implementation in the FE model. The extraction and preprocessing of joint reaction loads were performed for both walking and running.

The joint reaction loads were filtered in MATLAB to obtain relevant loads for the hip joint model considered. The selected relevant loads included loads exerted in the pelvis, hip and femur. The magnitudes of the pelvis loads were zero, thereby these loads were not used in the later analysis. Since the geometry of the FE model is composed of the left hip joint, only loads from the left hand side of the musculoskeletal model were considered. The stance phase of the walking and running cycle for the left femur was identified by applying a lower threshold of 10 Newton to the vertical ground reaction force. This threshold ensured detection of contact between the foot and the force plate, which characterizes the stance phase. The start position of the muscoloskeletal model in the identified stance phase for walking and running is illustrated in Figure 3.3. Thus, a time interval could be determined corresponding to these stance phases. The time interval was further used to extract the corresponding loads from the results of the joint reaction analysis. Furthermore, the time vector was shifted to set the initial time value to zero. The loads were later imported into the FE model by creating a text file that contained references to time-force respectively time-moment text files for each load in each direction. These text files contained time points in the first column with load values in the secound column separated by a comma. The same procedure was repeated to extract the hip flexion, hip adduction and hip rotation angles expressed in radians from the computed inverse kinematics data during the same stance phase for walking and running respectively.

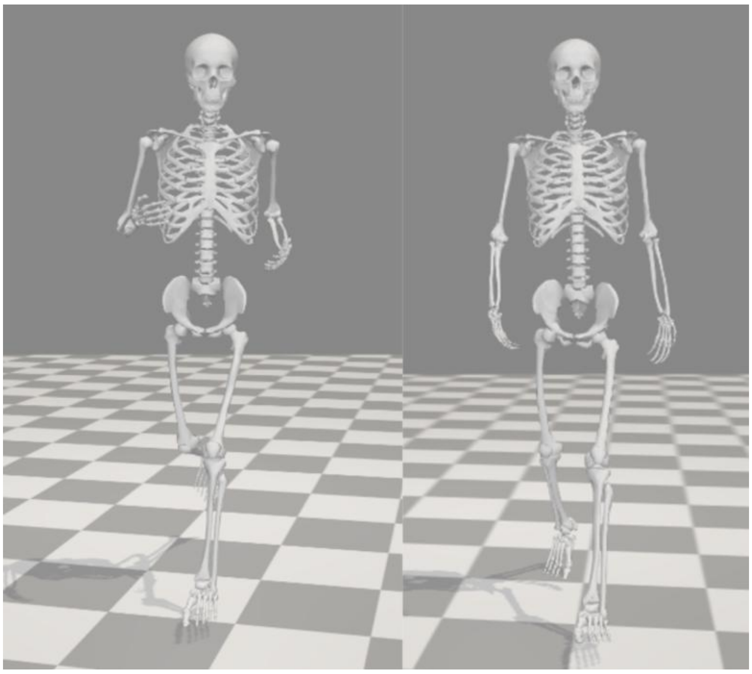

Figure 3.3: The scaled Catelli model is visualized in the start position of the experimental running cycle of the left leg to the left and the experimental walking cycle of the left leg to the right.

3.2 The Finite Element Model

This subsection presents the methodology used for the finite element modelling with subject-specific loading in this thesis. The same FE model with defined material properties and interactions was used for both walking and running stance, while different subject-specific boundary conditions were applied for each gait.

3.2.1 Material Models and Material Parameters

Since no CT or MRI images of the subjects were available, a FE model with a generic geometry of the left hip joint was used, which included the femur, the femoral cartilage, the acetabular cartilage and the ilium [56]. The model is illustrated in Figure 3.4. The femur and ilium were modelled as an isotropic linear elastic material, by which the Young's modulus was set to 17 GPa and the Poisson's ratio to 0.3. This material model is commonly used to model cortical bone in FE analysis [9], [22], [26], [57]. The acetabular and femoral cartilage were modelled as a neo-Hookean hyperelastic material, which capture the nonlinear stress-strain behaviour of cartilage [4], [5], [6], [25], [26], [27], [58]. In accordance with Equation (2.3) and Abraham et al., the parameter C_{10} was set to 2.043 MPa respectively D_1 was set to 0.051 MPa^{-1} [58]. First order tetrahedral elements (C3D4) with a median size of 2.5 mm were used to form the mesh of the whole FE model.

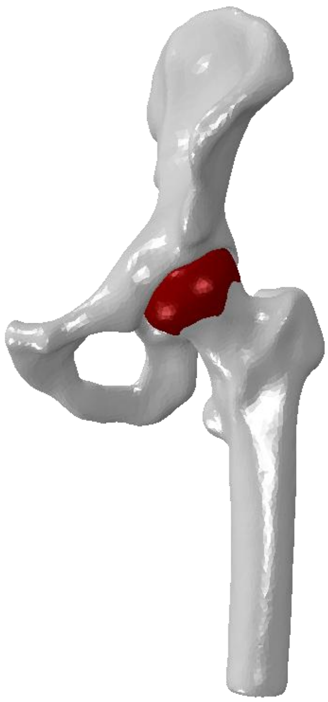

Figure 3.4: The FE model of the left hip joint is visualized, including the ilium and femur in grey respectively the acetabular cartilage and femoral cartilage in red.

3.2.2 Registration of FE Model to the Musculoskeletal Model

The FE model was registered to the musculoskeletal model to establish a consistent coordinate system between the musculoskeletal model and the FE model. Thus, the hip joint loads and kinematics computed in the musculoskeletal model could then be applied directly to the FE model.

The left femur geometry of the musculoskeletal model was exported using the software OpenSim Creator [59]. The musculoskeletal model was imported into the software. The corresponding geometry was further exported in the static position of the musculoskeletal model based on a reference system with an origin on the ground. The x axis of the reference system corresponds to anterior-posterior direction, the y axis superior-inferior direction and the z axis medial-lateral direction. The femur geometry was converted from meter to millimetre in MATLAB to ensure consistency with the unit system used in the FE model. Additionally, the geometry of the FE femur was exported from Abaqus. The registration of the FE model to the musculoskeletal model was performed in CloudCompare [60], in which the two geometries were imported. Initially, the two models were roughly aligned using the centroid of the respective model, yielding a first transformation matrix. Furthermore, four distinct reference points on and around the femoral head were manually identified in each model and used to align the two models relative one another. An additional transformation matrix was obtained from this procedure. Fine alignment was finally performed, which resulted in a third transformation matrix. Each transformation matrix was composed of a 4x4 matrix, by which the top-left 3x3 elements expressed rotations in all directions, the 3 elements in the fourth column expressed translations and the fourth row facilitated matrix multiplication.

Transformation of the FE nodal coordinates was performed in MATLAB. A text file containing all nodes in the FE hip joint model was loaded into the software. Additionally, a function was used to transform the number of nodes Nx3 array of FE nodes with the 4x4 transformation matrix, following the order of applied procedure in CloudCompare. Thus, transformed FE nodes were obtained, which correspond to the initial position of the hip joint in the musculoskeletal model. To verify alignment of the FE and musculoskeletal model, both geometries were plotted together in MATLAB. The alignment of the two models is visualized simultaneously in Figure 3.5. Furthermore, the transformed FE nodal coordinates were exported into a text file for later implementation in the FE model.

In the registered FE model, the x axis corresponded to anteriorly-posteriorly movement, the y axis superiorly-inferiorly movement and the z axis medially-laterally movement.

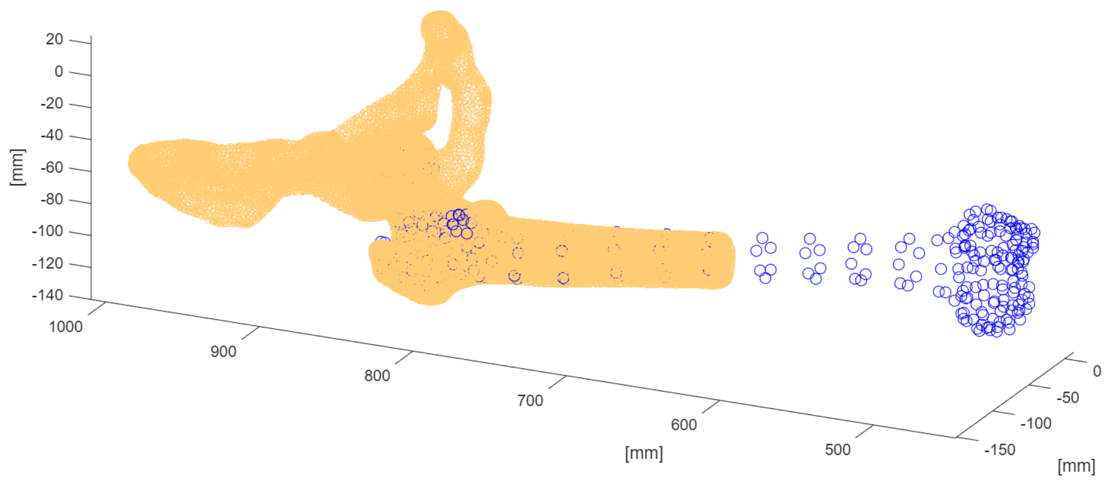

Figure 3.5: The alignment of the femur in musculoskeletal model illustrated in blue, and the FE hip joint model illustrated in orange. The x, y and z axis are expressed in millimetres.

3.2.3 Interactions and Contact Definition

After registration of the FE model to the musculoskeletal model, interactions and a contact definition were defined between the acetabular and femoral cartilage, mimicking the physiologically realistic hip joint mechanics.

Interactions and a contact definition were defined in the FE model to constrain the interfaces between the different parts of the model. A contact definition was established between the acetabular and femoral cartilage, replicating the contact mechanics between the cartilages. The contact between the cartilages was set to a surface-to-surface interaction, by which the acetabular cartilage illustrated the main surface and the femoral cartilage the secondary surface. Additionally, the contact was defined as frictionless and hard contact, preventing penetration of the two cartilages while allowing frictionless gliding. A reference point was created in the centre of the left femoral head, whose coordinates corresponded to the origin of the hip coordinate system in the musculoskeletal model. The reference point was further coupled to a node set on top of the ilium via an MPC coupling with a beam type. The coupling enabled controlling the movement of the ilium during the simulation.

3.2.4 Ligaments

Ligaments were used in the FE model to provide stabilization and maintain structural integrity of the parts included in the hip joint model. Four ligaments were implemented to mimic the hip joint capsule: the ichiofemoral, iliofemoral, pubofemoral and the teres ligament. The iliofemoral ligament was further divided into a superior and an inferior branch. The ligaments were represented by spring elements in the model. For the teres ligament, the location of the springs was selected to reproduce the characteristic star-shaped attachment points inside the acetabulum. Similarly, attachment points of the remaining springs in the model were chosen to replicate the anatomical locations of the respective ligament in the hip joint capsule. The number of spring elements and the corresponding spring stiffness were selected according to Zou et al., which could be seen in Table 3.2 [22]. Figure 3.6 illustrates the FE model where a few ligaments are visualized.

Ligament	Number of springs	Spring stiffness (N/mm)
Ichiofemoral	8	5
Inferior iliofemoral	6	17
Superior iliofemoral	6	16
Pubofemoral	6	6
Teres	6	12

Table 3.2: The number of springs and the respective spring stiffness for each ligament included in the FE model.

Figure 3.6: The FE hip joint model is visualized including a few ligaments. The reference point located in the centre of the femoral head is also illustrated with a yellow cross.

3.2.5 Boundary conditions

Boundary conditions were prescribed to constrain the FE model and reproduce the physiologically realistic movements during walking and running, respectively.

The used boundary conditions in the FE model were derived from the performed joint reaction analysis during walking respectively running stance, resulting in forces and moments in all directions. Additionally, the hip flexion, adduction and rotation angles obtained from the inverse kinematics analysis for each gait were used in the model as rotations. The joint reaction forces and rotations were applied on the reference point in the centre of the femoral head to control the movement of the ilium. The simulation was divided into two steps: a preload and a loading step. In the preload, the initial load values were applied as ramps. Additionally, the model was rotated to the heel strike of both gait cycles, creating a starting point for the loading step. The preload had a duration of 1 second in both simulations for the respective gait. The loading step had a duration of 0.29 seconds for walking stance and 0.23 seconds for running stance, mimicking the stance phase of the left femur for each gait. In this step, all obtained loads and rotations from the musculoskeletal model varied over time.

In the FE model, it was assumed that the ilium was moving around the femur, while the femur did not move. Hence, the distal end of the femur was fully fixed in both rotation and translation in all directions. The reference point inside the femoral head, that controls the ilium, was free to translate in all directions. Simultaneously, hip flexion/extension, adduction/abduction and internal/external rotation angles were prescribed at the reference point in the respective rotational direction. Since the ilium was moving, the inversed hip flexion and hip rotation angle were applied, while the hip adduction angle was kept in its original form to obtain consistent simulation with the musculoskeletal model.

3.2.6 Numerical Solver Settings

After establishing material properties and boundary conditions of the FE model for each gait, solver settings were specified for the numerical analysis.

The FE simulations were performed in Abaqus/Standard. To account for large deformations during the simulations, nonlinear geometry effects and unsymmetrical matrix storage were defined in the preload and loading steps. Automatic time incrementation was applied with an initial increment size of 0.01 for the preload step respectively 0.001 for the loading step. The maximum increment size was selected in accordance with the duration of the respective step with a value of 1 for the preload step and 0.29 for the loading step in the walking simulation and 0.23 in the running simulation. For both steps, the minimum increment size was set to 1×10^{-8} and the maximum number of increments was limited to 10 000. Furthermore, automatic contact stabilization with a factor of 0.15 was applied in the beginning of the loading step at the cartilage contact interface to improve numerical stability and facilitate convergence of the numerical solution.

4 Results

This section describes the results from the musculoskeletal modelling part followed by the results from the finite element part with subject-specific loading. The results include hip kinematics, a ground reaction force graph, joint reaction loads, stress and strain graphs, load distribution figures and a contact area graph.

4.1 The Musculoskeletal Model

This subsection presents the results of the musculoskeletal modelling for both walking and running, including hip kinematics, ground reaction force, hip joint reaction forces and moments.

The hip joint kinematics reproduced the experimental marker trajectories with a mean root mean square (RMS) error of 24.46 mm and 21.1 mm across the analysed walking and running trial respectively. The RMS errors range from 18.87 mm to 26 mm for walking and from 16.2 mm to 26.9 mm between frames for running. The maximum marker error reached a value of 27.26 mm for walking and 55.7 mm for running. The hip flexion/extension, adduction/abduction and internal/external rotation angles are illustrated simultaneously in Figure 4.1 for the analysed walking and running cycle respectively. The positive y values indicate hip flexion, adduction and internal hip rotation, while the negative y values correspond to extension, abduction and external rotation of the hip. The FE model was driven by the kinematics from 0-35 % of both cycles, corresponding to the stance phase.

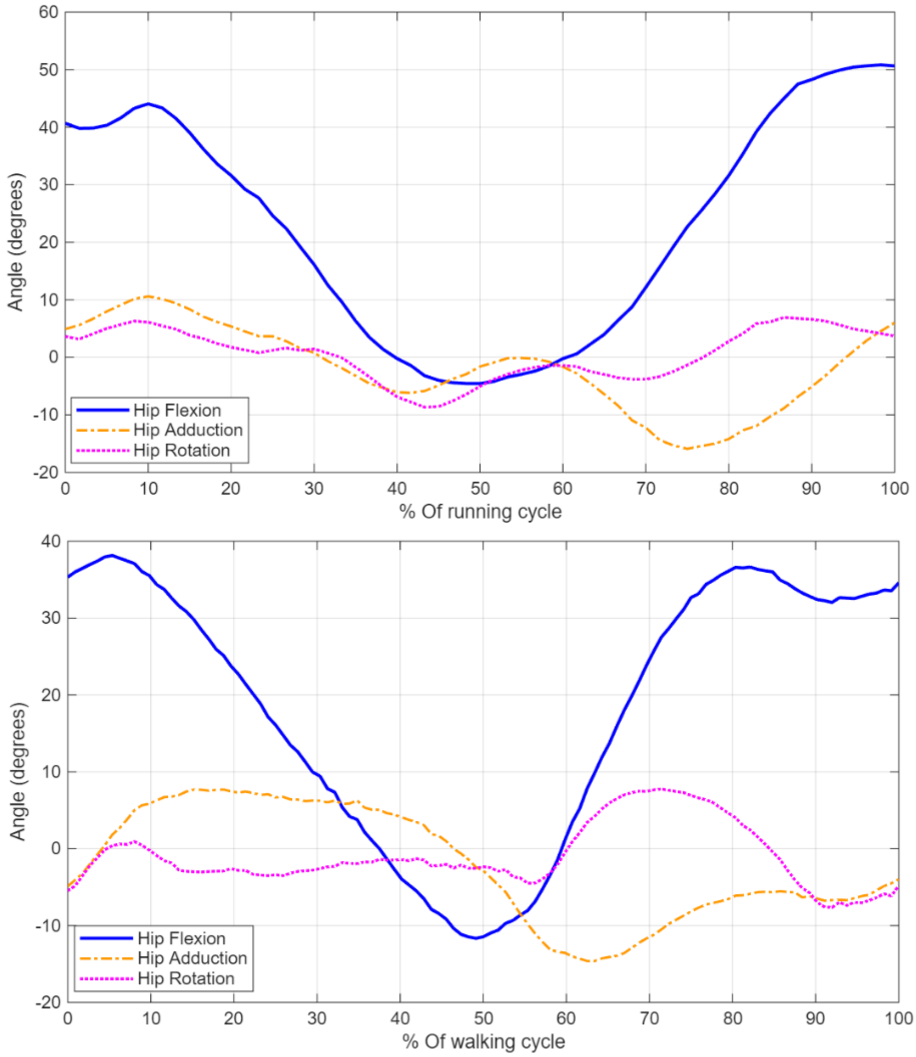

Figure 4.1: Joint angles obtained from the inverse kinematic analysis for the full running cycle (top row) and the full walking cycle (bottom row). The rotations applied on the FE hip joint model corresponds to 0-35 % of the respective cycle, representing the stance phase. The hip flexion angle is shown in blue, the hip adduction angle is shown in yellow and the hip rotation angle is shown in pink.

The vertical ground reaction force is illustrated in Figure 4.2. The positive y values indicate the vertical force directed downwards obtained from the interaction between the left foot and the force plate in the treadmill throughout the stance phase. The ground reaction force for walking exhibits an initial loading peak occurring around 1.3 BW at approximately 10 % of the stance phase followed by a second loading peak occurring at approximately 44 % of stance phase. For running, the ground reaction force exhibits the characteristic smaller peak occurring around 2 BW at approximately 10 % of the stance phase followed by a greater peak occurring around 2.4 BW at approximately 44 % of the stance phase.

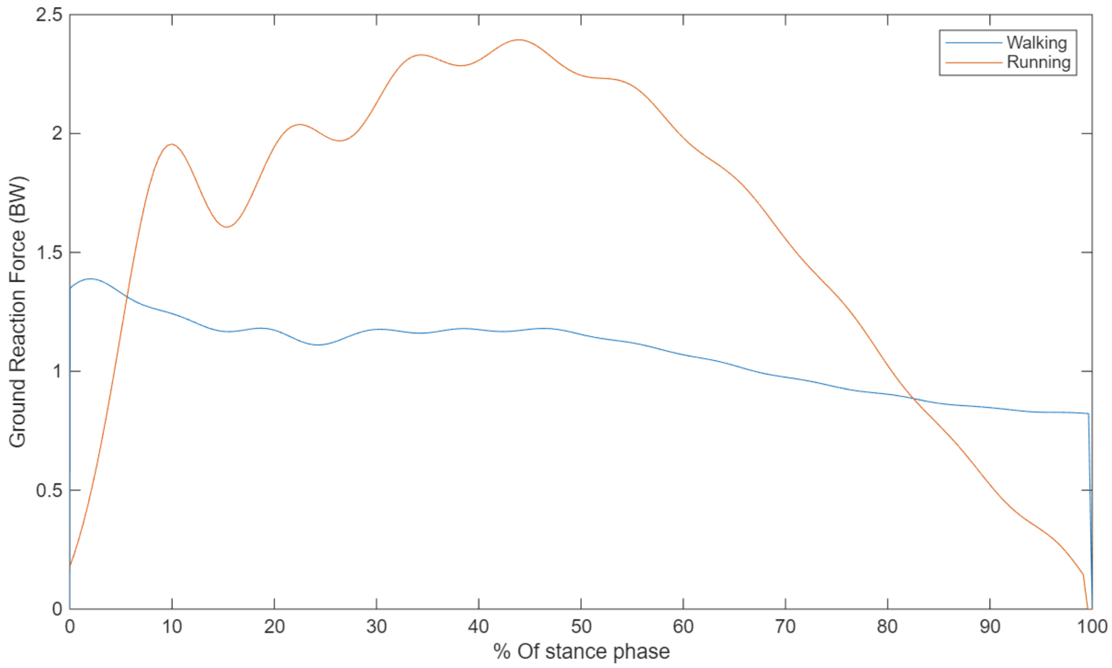

Figure 4.2: The ground reaction force in y direction obtained from the contact between the left foot of the subject and the force plate in the treadmill during the stance phase for the considered running cycle in orange and the walking cycle in blue.

The computed hip joint reaction forces from the joint reaction analysis are visualized in Figure 4.3 for walking and running, along with the resultant of the forces throughout the stance phase. The joint reaction force in the x direction represent anterior-posterior movement, the y-component corresponds to superior-inferior movement and the z-component represents medial-lateral movement. Positive y values indicate anterior, superior and medial movements, while negative y values correspond to posterior, inferior and lateral movements. The superior-inferior component acting on the femur demonstrates the largest joint reaction force component throughout the stance phase in both running and walking, see Table 4.1 and 4.2. For walking, a significant peak in the resultant joint reaction force was observed from 1.5 MPa to 15.9 MPa at approximately 5 % of stance. A second force peak occurs from 6.8 MPa to 12 MPa at approximately 20 % of stance. For running, the resultant joint reaction force exhibits a substantial peak in force from 2.8 MPa to 10.7 MPa at approximately 36 % of stance. Two additional peaks are observed from 2 MPa to 10 MPa at approximately 10 % of stance and from 6.1 MPa to 9.6 MPa at approximately mid-stance.

The joint reaction moments varied over stance in both gaits, which are illustrated simultaneously in Figure 4.4. For walking, a substantial initial peak in the medial-lateral moment (M_x) is observed at -225 Nm. An additional initial peak in the anterior-posterior moment (M_y) is shown at -140 Nm followed by a second moment peak around -123 Nm at 10 % of stance. A moment peak in the superior-inferior moment (M_z) is observed around -76 Nm at 14 % of stance. The moment components remain stable throughout the walking trial after 22 % of stance: approximately $\pm$ 0.5 Nm for the medial-lateral moment (M_x), $\pm$ 0.06 Nm for the anterior-posterior moment (M_y) and $\pm$ 0.9 Nm for the superior-inferior moment (M_z). For running, a pronounced peak in the medial-lateral moment (M_x) from -4 Nm to 37 Nm is demonstrated at approximately 52 % of the stance phase. The other moment components show substantially lower variations in magnitude: approximately $\pm$7 Nm for the anterior-posterior moment (M_y) and $\pm$10 Nm for the superior-inferior moment (M_z).

Force component	Maximum value (BW)	Minimum value (BW)
Anterior-Posterior (F_x)	2.78	-1.61
Superior-Inferior (F_y)	-1.27	-9.46
Medial-Lateral (F_z)	0.12	-2.26

Table 4.1: The maximum and minimum values for the joint reaction forces in running stance are illustrated in BW for each force component.

Force component	Maximum value (BW)	Minimum value (BW)
Anterior-Posterior (F_x)	5.74	0.077
Superior-Inferior (F_y)	-1.33	-14
Medial-Lateral (F_z)	-0.58	-3.7

Table 4.2: The maximum and minimum values for the joint reaction forces in walking stance are illustrated in BW for each force component.

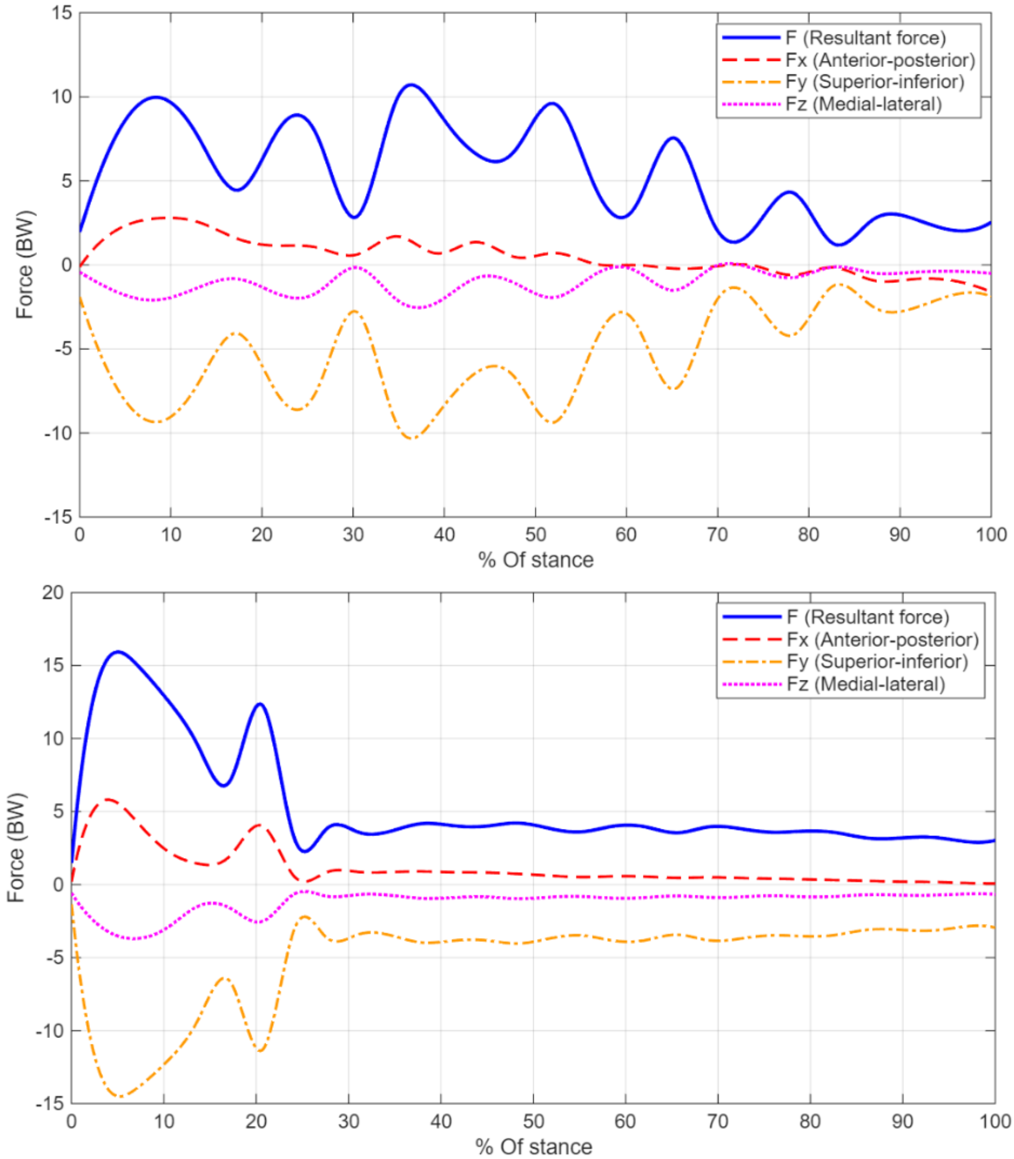

Figure 4.3: The forces applied to the reference point in the FE hip joint model in x, y and z direction with respect to the percent of the stance phase in running (top row) and walking (bottom row). The resultant of the three forces for the respective gait is illustrated in blue. The force in x (anterior-posterior) direction is shown in red, the force in y (superior-inferior) direction in yellow and the force in z (medial-lateral) direction in pink.

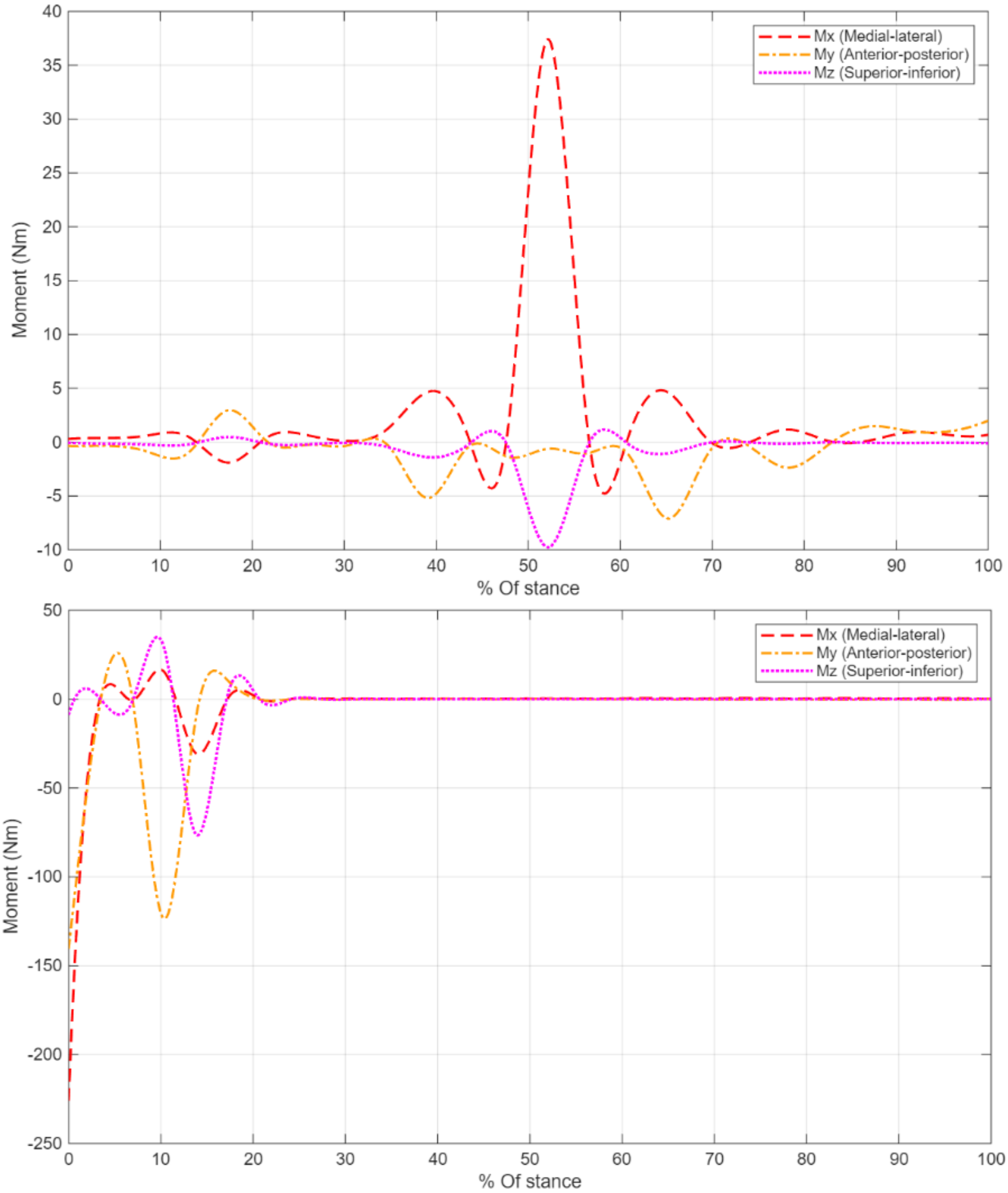

Figure 4.4: The moments during stance phase in running (top row) and in walking (bottom row) obtained from the joint reaction analysis performed. The moment in x (medial-lateral direction) is shown in red, the moment in y (anterior-posterior direction) is illustrated in yellow and the moment in z (superior-inferior direction) is shown in pink.

4.2 The Finite Element Model

This subsection presents the results of the finite element simulation for walking and running, including load graphs, distribution figures and a contact area graph.

The mean and 99th percentile of the von Mises stress and the maximum of principal strain within the acetabular cartilage as a function of time are visualized for running in Figure 4.5 and for walking in Figure 4.6. For the simulated stance phase in walking, a substantial peak in von Mises stress is observed from 4.5 MPa at initial heel strike (1 % of stance) to 11 MPa at 3.6 % of stance. The von Mises stress then stabilizes around 11-10 MPa. This time point occurs in correspondence to the first peak in ground reaction force. After the second peak in ground reaction force (44 % of stance) around 9.9 MPa the von Mises stress gradually decreases toward toe-off. Initially, a rapid increase in von Mises stress during the running simulation occurs from 7 MPa at approximately 1 % of stance to 11 MPa at 10 % of stance followed by a peak of 13.5 MPa at mid-stance. The peak von Mises stress occurs in correspondence of the second peak in the ground reaction force in Figure 4.2. The von Mises stress further gradually decreases from 13.5 MPa at mid-stance to 2 MPa toward the toe-off phase of the stance phase.

For both gaits, the maximum principal strain follows a similar behaviour as the von Mises stress. However, the initial peak in strain around 0.4 for walking is more pronounced compared to the pattern observed in the von Mises stress. For both gaits, the variations in the FE response in Figure 4.5 and 4.6 are consistent with the fluctuations in the hip joint reaction forces in Figure 4.3.

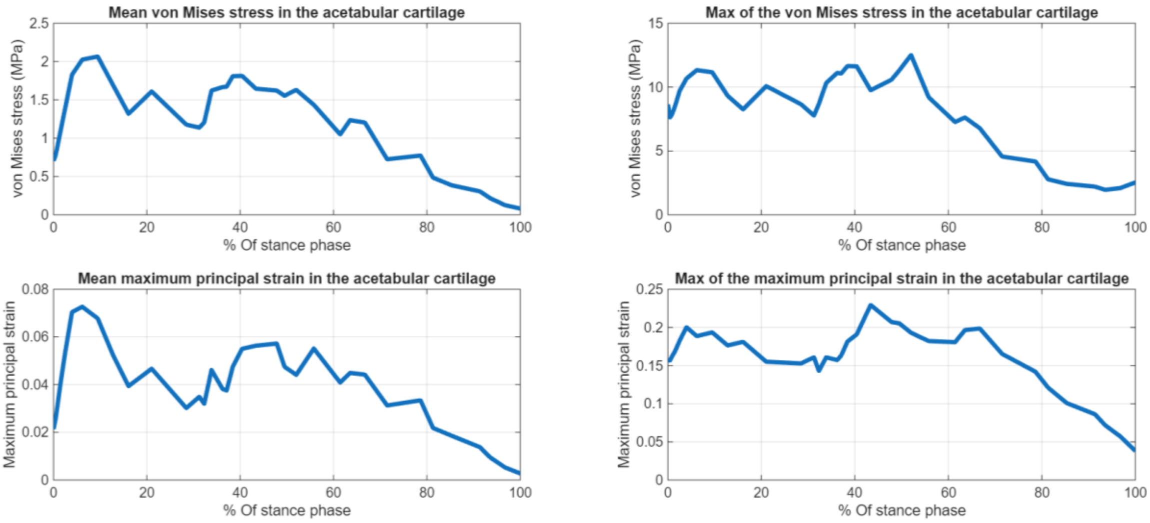

Figure 4.5: The mean and 99th percentile of von Mises stress and maximum principal strain in the acetabular cartilage obtained in the FE simulation for the analysed stance phase in running. The two top graphs show the von Mises stress and the two bottom graphs show the maximum principal strain.

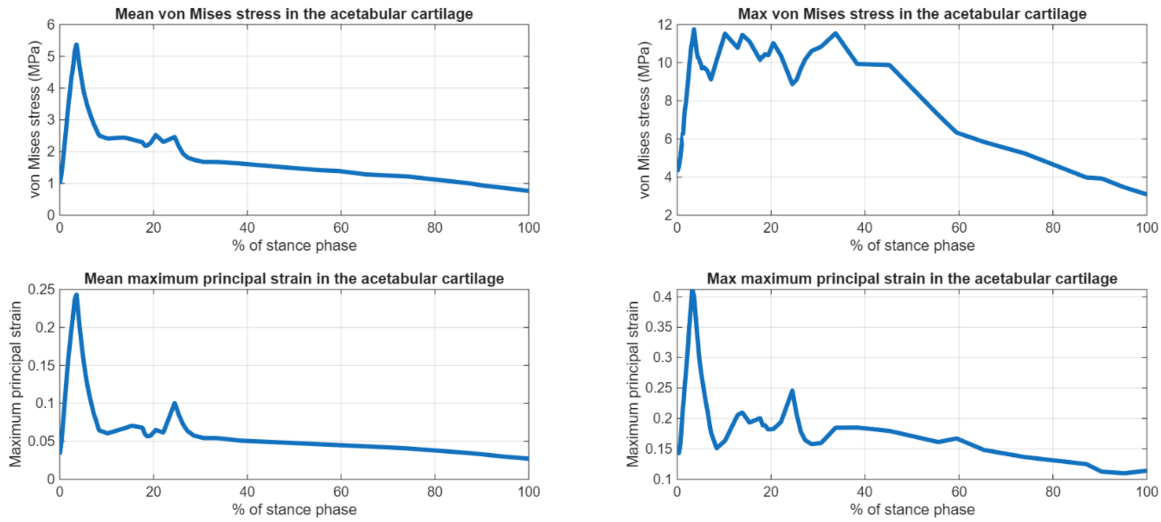

Figure 4.6: The mean and 99th percentile of von Mises stress and maximum principal strain in the acetabular cartilage obtained in the FE simulation for the analysed stance phase in walking. The two top graphs show the von Mises stress and the two bottom graphs show the maximum principal strain.

The spatial distribution of von Mises stress, contact pressure and maximum principal strain within the acetabular cartilage are illustrated in Figure 4.8, 4.10 and Supplementary Figure 8.2 for the simulated walking stance and in Figure 4.7, 4.9 and Supplementary Figure 8.1 for the simulated running stance. For walking, each figure visualizes the loading patterns occurring at the initial heel strike, the first and second peak in ground reaction force and at mid-stance. For running, each figure illustrates the loading patterns occurring at the first and second peak in ground reaction force and the time point during the maximum von Mises stress.

For walking, a pronounced concentration of von Mises stress occurs in the superior-posterior region during the first peak in ground reaction force, which corresponds to the maximum von Mises stress during the simulated walking. The region of the concentration is in correspondence to the one in the simulated running. The concentration becomes more localized in the second peak in ground reaction force. Less pronounced concentrations are observed during initial heel strike and mid-stance, shown in Figure 4.8. For running, during the first peak in ground reaction force (10 % of the stance phase), a pronounced concentration of von Mises stress is observed in the superior-posterior region of the acetabular cartilage (Figure 4.7). Similarly to walking, this region becomes more localized at the second peak in ground reaction force (44 % of the stance phase). The maximum von Mises stress occurred during mid-stance.

For walking, the highest contact pressure is observed with a magnitude of 30.5 MPa in the first and second ground reaction force (Figure 4.10). The location of the concentration is in correspondence to the one in running with a more inferiorly region during the first peak in ground reaction force. The region becomes more localized during the second ground reaction and less pronounced during mid-stance. The contact pressure is least distinct in the initial heel strike. For running, the contact pressure pattern within the acetabular cartilage exhibits similar distribution as the von Mises stress, see Figure 4.9. The highest contact pressure occurring at the first peak in ground reaction force is observed with a magnitude of 33.7 MPa in the superior region of the cartilage. It remains at this location throughout the stance phase. During the mid-stance, the contact pressure increased further.

For walking, the maximum principal strain field is more diffusely distributed during the initial heel strike and the first peak in ground reaction force. The strain becomes more superiorly localized at a magnitude of 0.4 during the second peak in ground reaction force and mid-stance, see Supplementary Figure 8.2. For running, the maximum principal strain field is more broadly distributed at the first and second peak in ground reaction force. Similarly to walking, it further emerges toward superior regions and becomes more localized at a magnitude of 0.25 during the time point for the maximum von Mises stress, see Supplementary Figure 8.1.

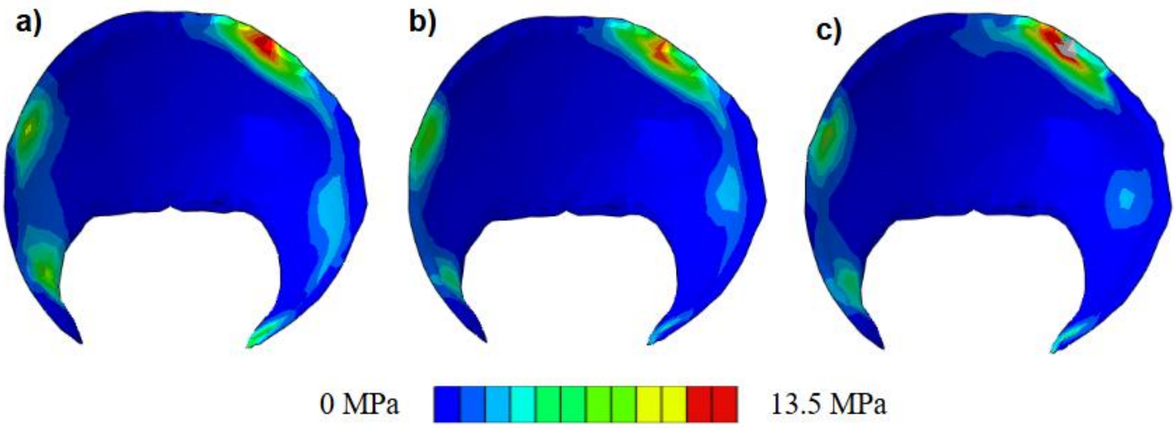

Figure 4.7: The load distribution of the von Mises stress in the acetabular cartilage during running stance at a) the first peak of the ground reaction force (10 % of the stance phase), b) the second peak in the ground reaction force (44 % of the stance phase) and c) the maximum von Mises stress (50 % of the stance phase).

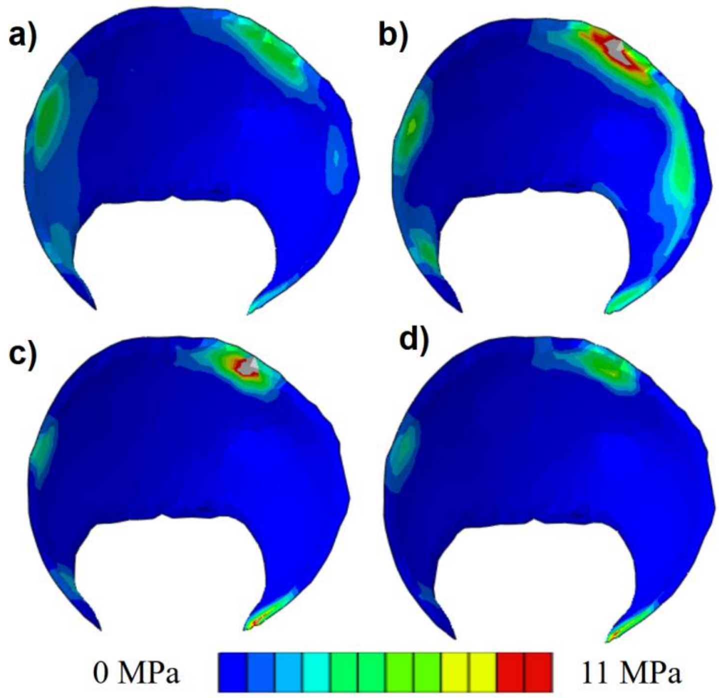

Figure 4.8: The load distribution of the von Mises stress in the acetabular cartilage during walking stance at a) the initial heel strike (1 % if stance phase) b) the first peak of the ground reaction force (10 % of the stance phase), c) the second peak in the ground reaction force (44 % of the stance phase) and d) mid-stance (50 % of the stance phase).

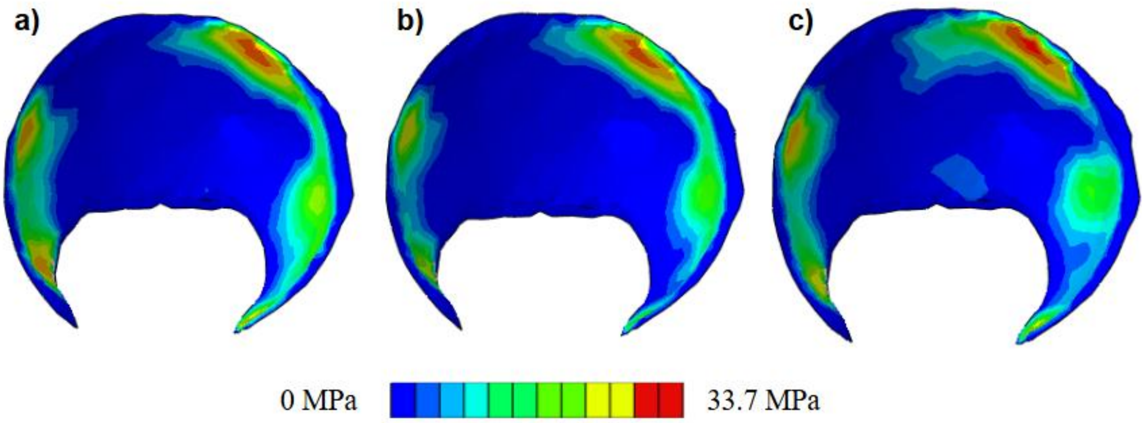

Figure 4.9: The load distribution of the contact pressure in the acetabular cartilage during running stance at a) the first peak of the ground reaction force (10 % of the stance phase), b) the second peak in the ground reaction force (44 % of the stance phase) and c) the contact pressure at the maximum von Mises stress (50 % of the stance phase).

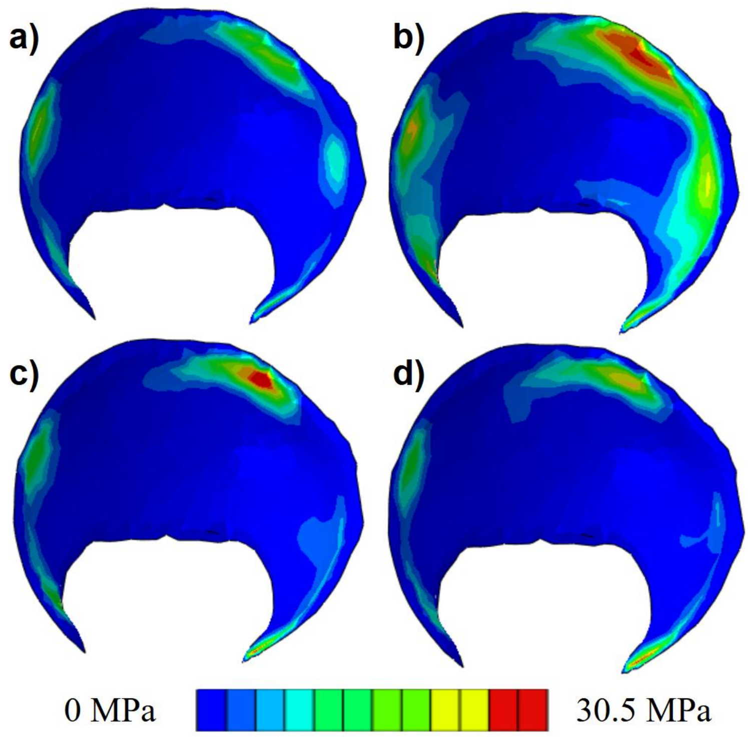

Figure 4.10: The load distribution of the contact pressure in the acetabular cartilage during walking stance at a) the initial heel strike (1 % if stance phase) b) the first peak of the ground reaction force (10 % of the stance phase), c) the second peak in the ground reaction force (44 % of the stance phase) and d) mid-stance (50 % of the stance phase).

The variation in acetabular cartilage contact area throughout the stance phase for walking and running is illustrated together in Figure 4.11. For walking, an initial rapid increase in contact area is observed from 354 mm^2 at heel strike to 608 mm^2 at 5 % of stance. The contact area remained then relatively stable around 430 mm^2. The contact area during the stance phase in walking at the initial heel strike, first and second peak in ground reaction force along with mid-stance is shown in Table 4.4. After mid-stance, a gradually reduction in contact area occurred from 430 mm^2 to 300 mm^2 toward toe-off. For running, a similar rapid increase in contact area is initially observed from 380 mm^2 at initial heel strike to 549 mm^2 at 10 % of stance, corresponding to the first peak in ground reaction force. The contact area subsequently remained relatively stable around 530 mm^2. The contact area at the first and second peak in ground reaction force along with the time point corresponding to the maximum von Mises stress is shown in Table 4.3. After mid-stance, a reduction in contact area is observed from 508 mm^2 at mid-stance to 14 mm^2 toward the toe-off phase.

Time point	Stance phase (%)	Contact area (mm^2)
1st GRF peak	10	549
2nd GRF peak	44	523
Maximum von Mises stress	50	508

Table 4.3: The contact area in running stance at the first and second peak in ground reaction force and at the time point corresponding to the maximum von Mises stress.

Time point	Stance phase (%)	Contact area (mm^2)
Initial heel strike	1	442
1st GRF peak	10	573
2nd GRF peak	44	427
Mid-stance	50	425

Table 4.4: The contact area in walking stance at the initial heel strike, the first and second peak in ground reaction force and at mid-stance.

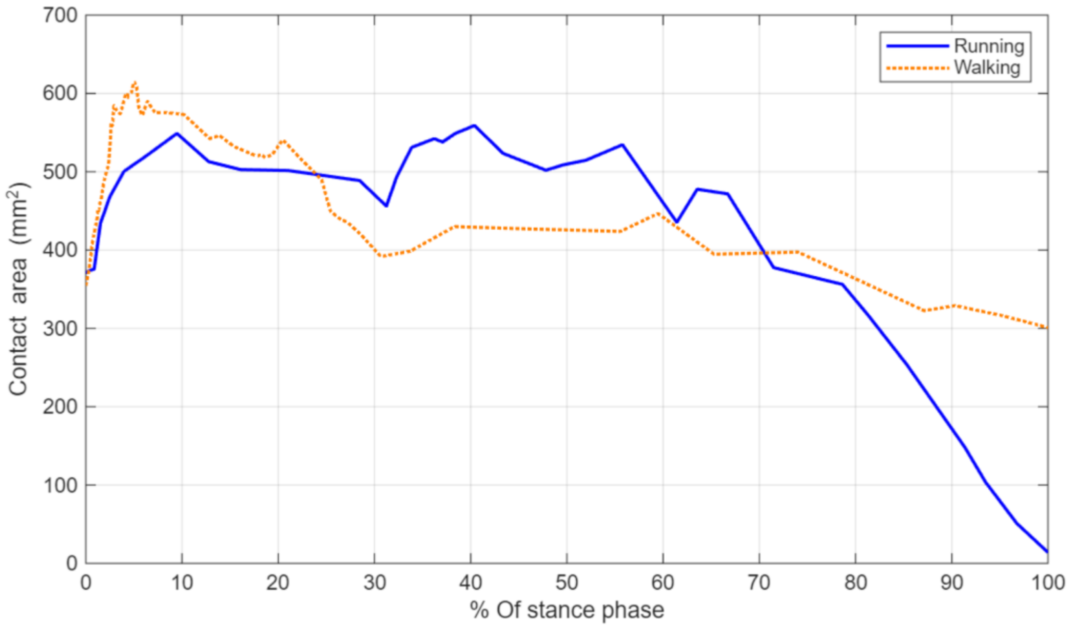

Figure 4.11: Acetabular cartilage contact area throughout the simulated stance phase in running (blue) and walking (orange). The contact area is expressed in square millimetres (mm^2).

5 Discussion

This master's thesis aimed at developing a pipeline that could enable investigation of stress distributions within the hip joint during walking and running in a subject-specific fashion. This was achieved by developing a pipeline that combined musculoskeletal models and finite element modelling. The pipeline reproduces experimental motion capture data in a musculoskeletal model to extract joint reaction forces acting within the hip. The extracted forces and rotations are subsequently implemented into a finite element model of the hip joint to simulate the stance phase of a gait cycle, enabling evaluation of stress distributions in the acetabular cartilage.

5.1 The Musculoskeletal Model

Although minor deviations and oscillations were observed, the ground reaction force profiles for both walking and running are generally consistent with previous published literature [61], [62]. This suggests that the experimental data that was used as input for the musculoskeletal modelling analyses provide a realistic representation of gait loading.

The ground reaction force obtained from the experimental data for walking and running in Figure 4.2 is comparable to the those reported by Uchida and Delp shown in Figure 5.1 [62].

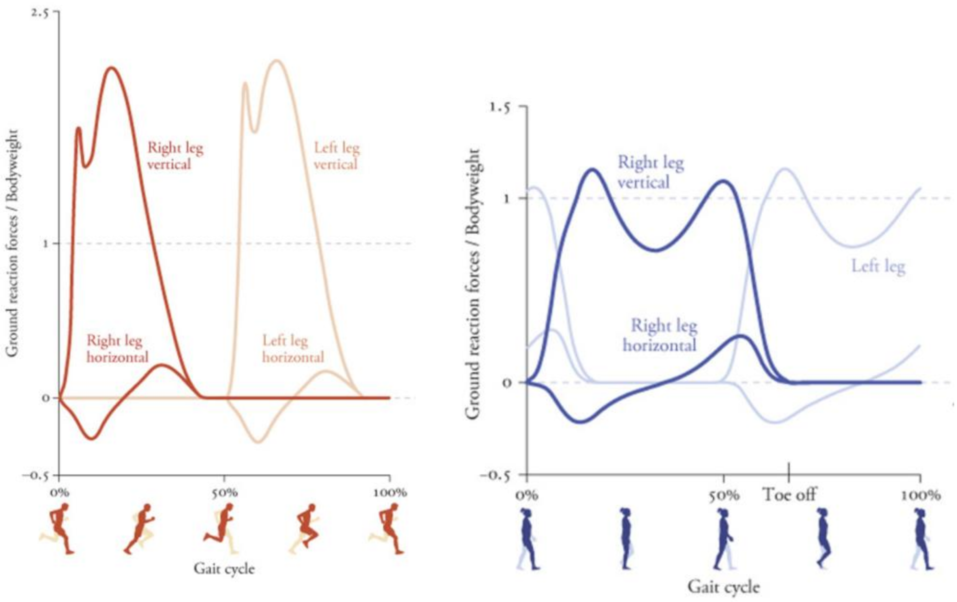

Figure 5.1: The vertical and horizontal ground reaction force for running when landing on the heel (left) and walking (right). Adapted from [62].

For both gaits, the vertical ground reaction force profiles by Uchida and Delp demonstrated similarities in shape and magnitude compared to Figure 4.2. For walking, the characteristic M-shaped vertical ground reaction force pattern in Figure 4.2 is less clearly defined with an attenuated second peak compared to the one reported by Uchida and Delp shown in Figure 5.1. Despite the M-shaped force profile, the range in magnitude is similar in the two graphs (peak force ~1.2-1.3 BW). However, unlike the ground reaction force profile for walking reported by Uchida and Delp in Figure 5.1, the present study exhibited a rapid increase during the initial heel strike and a rapid decrease during toe-off. A more gradual change was reported by Uchida and Delp in Figure 5.1. This difference may indicate issues associated with the recording of the initial contact and toe-off phase during the walking trial. For running, the ground reaction force in Figure 4.2 and the one reported by Uchida and Delp in Figure 5.1 exhibit a similar characteristic first loading peak around 2 BW at 10 % of stance associated with landing on the heel during running. Additionally, the magnitudes in the two graphs are in the same range throughout the stance phase of running with the peak forces between 2 and 2.5 BW [62].

Giarmatzis et al. calculated hip joint contact forces for walking and running at different speeds through musculoskeletal modelling based on motion capture data for 20 participants to offer insights in musculoskeletal loading during the two gaits [61]. When comparing the ground reaction forces collected for the present study and those from Giarmatzis et al., it was observed again similar force profiles and magnitudes, except for the already discussed rapid change in initial heel strike and toe-off during walking in the experimental data [61].

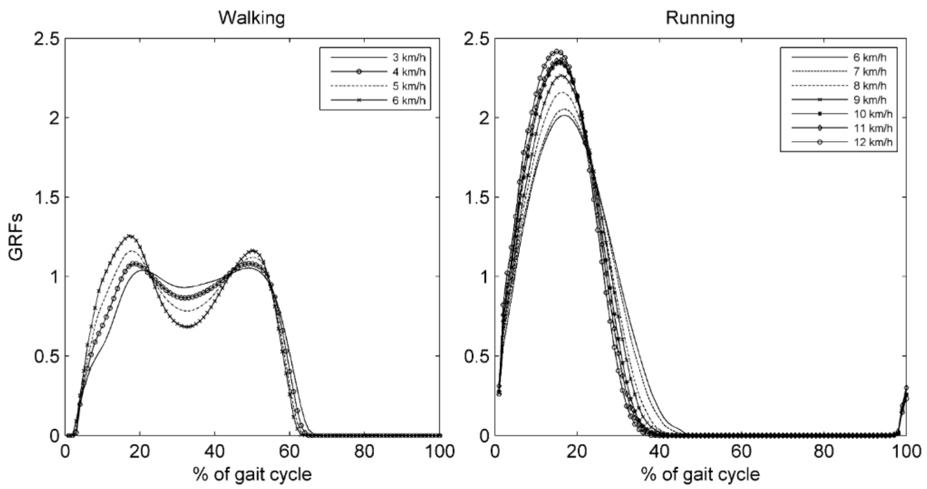

Figure 5.2: The ground reaction force throughout a whole gait cycle at different speeds during walking (left) and running (right). Adapted from [61].

Also, the ground reaction forces from Giarmatzis et al. did not show a first loading peak during running (Figure 5.2) [61]. The absence of the first loading peak during running might be explained by differences between the subjects in foot strike pattern during the trials reported by Uchida and Delp [62]. However, both Giarmatzis et al. and Uchida and Delp exhibit smoother force profiles and do not report the oscillations that was recorded in the experimental data during walking and running in Figure 4.2 [61], [62]. It is likely that such oscillations originate from the mechanical vibrations and noise associated with the treadmill used for experimental trials, thereby affecting the force plate measurements.

Despite the offset in hip rotation angle during running, the computed hip kinematics in the present study demonstrated good agreement with previously published walking and running data in terms of waveform characteristics and joint angle magnitudes [63], [64]. This suggests that the computed hip kinematics provide physiologically realistic representations of each gait.

In a study by Chandra et al. the kinematics of 100 participants was recorded during walking [63]. A study by Schache et al. compared changes between overground and treadmill running in 3D angular kinematics of lumbo-pelvic-hip complex by using ten participants [64]. The computed hip kinematics for walking and running in Figure 4.1, including hip flexion, adduction and internal rotation angles, show comparable waveform characteristics and magnitude to those reported by Chandra et al. (Figure 5.3) and Schache et al. (Figure 5.4), indicating consistency with those studies performed on large cohorts [63], [64].

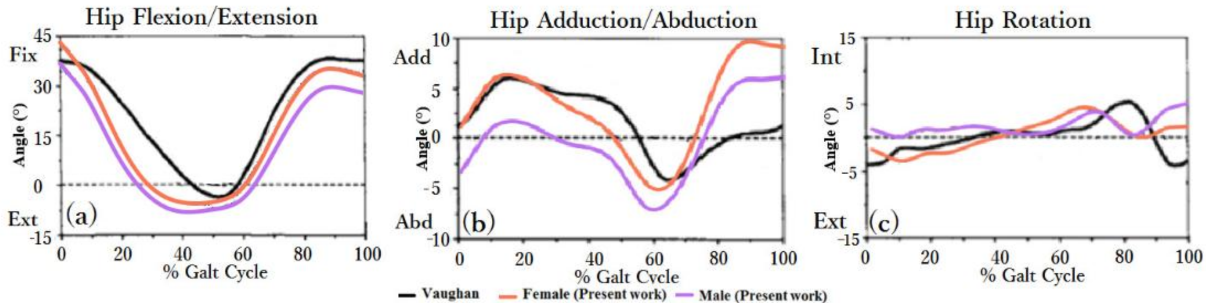

Figure 5.3: The hip kinematics including hip flexion/extension, adduction/abduction and internal/external rotation for a walking cycle. Adapted from [63].

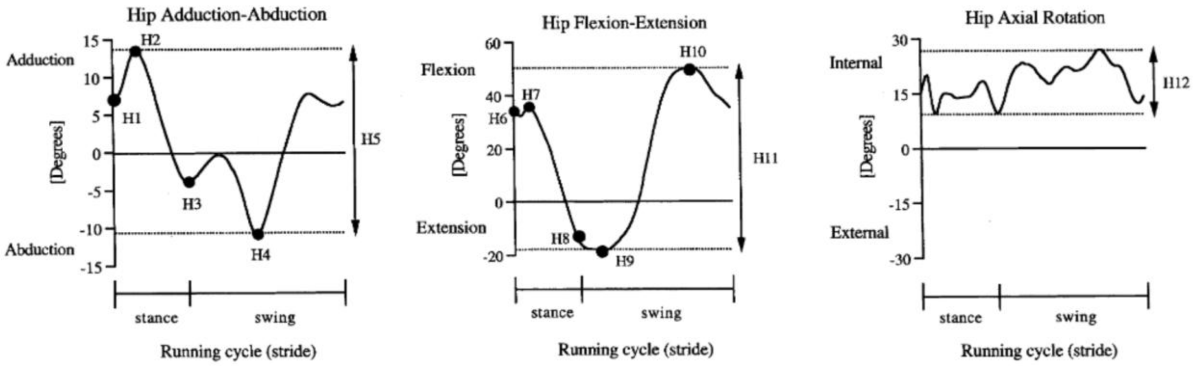

Figure 5.4: The hip kinematics including hip flexion/extension, adduction/abduction and internal/external rotation for a running cycle. Adapted from [64].

The hip flexion angle in both gaits exhibits an overall similarity in pattern with Chandra et al. and Schache et al. [63], [64]. For walking, identical hip flexion angles were reported by Chandra et al. throughout the cycle, particularly during initial heel strike (approximately 40°), the minimum (approximately -10°) respectively the second peak (approximately 40°) in hip flexion [63]. For running, the first peak was slightly higher in the present study (43°) compared to Schache et al. (40°). A larger difference was observed in the minimum flexion angle with -5° in the present study and -20° reported by Schache et al. (Figure 5.4). The second peak in flexion angle was comparable in both studies, reaching 50° [64].

For both gaits, the hip adduction angle also exhibits a consistent overall waveform with the those reported by Chandra et al. and Schache et al. [63], [64]. For walking, the first and second peak in hip adduction of 8° and -5° were comparable to those reported by Chandra et al. of 7° and 0°, respectively. A more pronounced variability was observed at the minimum hip adduction angle with a value of -12° in the present study and -5° reported by Chandra et al [63]. For running, a slight difference was observed at the first peak (10°) and second minimum (-15°) in adduction angle in the present study compared to 14° and -11° reported by Schache et al., respectively. Both the first minimum and second peak were highly comparable between the studies [64].

For walking, the internal hip rotation angle was comparable to the one reported by Chandra et al., with identical angle (-2°) at 20 % of the analysed cycle and a slight difference in angle of 1° at 70 % and 95 % of the analysed cycle [63]. For running, despite similar overall shapes, the internal hip rotation angle recorded in the experimental data was approximately -15° less compared to the values reported by to Schache et al [64]. The offset may result from deviations in determining the medial-lateral axis used when defining the femoral coordinate system. This is not completely surprising, considering that hip rotation angles are considered among the least repeatable parameters in gait analysis [65].

Although fluctuations and prominent force peaks were observed, the overall hip joint reaction force magnitudes and waveform characteristics were comparable to previous published musculoskeletal modelling and in vivo studies [61], [66], with peak forces of approximately 4 BW for walking and 8 to 9 BW for running.

Despite the fluctuations observed in Figure 4.3, the resultants of the hip joint reaction forces for walking and running are consistent with the force profiles reported by Giarmatzis et al. from 0 to 35 % of the gait cycle, corresponding to the stance of walking and running respectively (Figure 5.5).

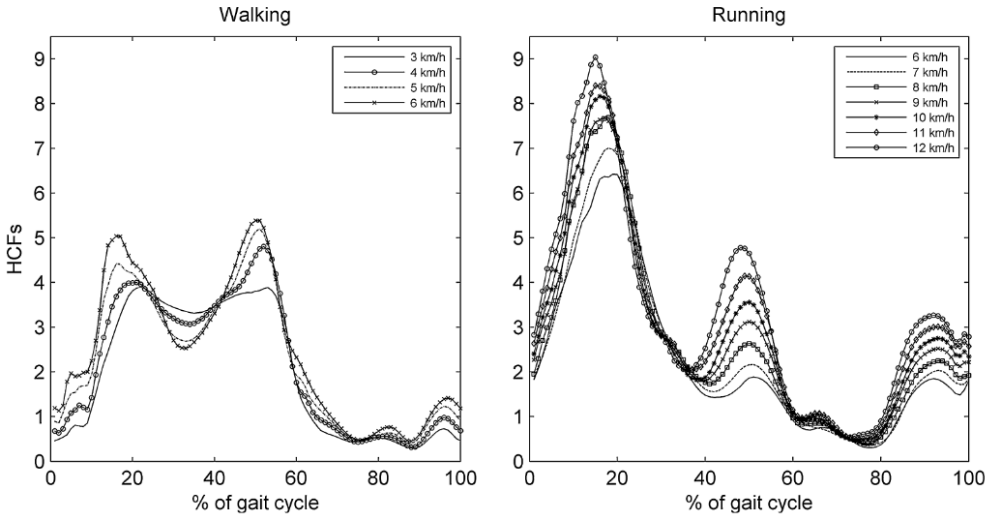

Figure 5.5: The resultant of hip contact forces throughout a whole gait cycle at different speeds during walking (left) and running (right). Adapted from [61].

For walking, the overall resultant hip joint reaction force profile is comparable to the one reported by Giarmatzis et al. at the same speed (5 km/h) with a reduction in force toward the toe-off phase. However, the two prominent peaks in the resultant of joint reaction force of 15.9 BW and 10.7 BW reported in this study (Figure 4.3) are not present in the study by Giarmatzis et al. (Figure 5.5). This was believed due to a series of artefacts in the present modelling methodology for the musculoskeletal models, as detailed later in this report. Although peaks were present from 0 % to 20 % of walking stance in this study, the magnitudes of each force components for the remainder stance phase were comparable to Giarmatzis et al. around -1.5 BW, -4 BW and -1 BW for the x, y and z force component, respectively. As running, the resultant of the joint reaction forces exhibits a slightly higher magnitude compared to Giarmatzis et al. at a comparable speed of running (11 km/h). Two additional higher peaks approaching 10 BW can be identified in the present study but were not reported by Giarmatzis et al. Overall both the present study and Giarmatzis et al. reported similar peak magnitudes of approximately 8 to 9 BW and a vertical force of approximately 2 BW during the toe-off phase. Both the x (anterior-posterior) and z (medial-lateral) force component are comparable to Giarmatzis et al. around 3 BW and -2 BW respectively. However, a noticeable difference can be observed in the y (superior-inferior) force component with one peak of -10 BW at approximately 35 % of the stance phase. Despite this peak, the magnitude of the force component is generally comparable to Giarmatzis et al., reaching approximately 8 BW [61].

Bergmann et al. measured in vivo hip joint contact forces from instrumented hip implants in two subjects during walking and running. During walking at 5 km/h, a peak resultant force of 3.94 BW was found. Except for the initial force peak observed in Figure 4.3, this value is highly comparable to the approximately 4 BW observed in the present study at identical speed of 5 km/h. However, during running at 7 km/h, Bergmann et al. reported peak resultant force of 5.5 BW [66], which is approximately 50 % smaller than those reported in the present study, where the running speed was 10.5 km/h. The differences in gait mechanics, i.e. performance and running speed, could therefore explain the difference in hip joint contact forces. Giarmatzis et al. also reported a speed-dependent increase in hip contact force using musculoskeletal modelling (Figure 5.5) [61]. Additionally, differences in subject and methodology should be considered. Bergmann et al. measured forces in elderly subjects with instrumented hip implants, while the present study computed the hip joint reaction forces through musculoskeletal modelling in young populations.

None of the studies found in literature exhibited fluctuations in the hip joint contact forces like those it was obtained in the present analysis (Figure 4.3). It could indeed be believed that such oscillations are not realistic and additional work is ongoing to try to pinpoint the reasons behind such oscillations. Since the kinematics data (Figure 4.1) did not feature significant oscillations or noise for neither walking nor running, the oscillations in hip joint reaction force might result from later steps in the analyses in the musculoskeletal modelling, particularly static optimization and joint reaction analysis. Those analyses include indeed inputs from the recorded ground reaction force, which presented some noise and oscillations. However, a preliminary attempt at filtering out the noise from the ground reaction force resulted in a minimal improvement in joint reaction forces observed compared to Figure 4.3.

Another possible explanation for the oscillations in the joint contact forces could be that the presented models do not correctly capture the different muscle contributions during the static optimization phase. According to Hicks et al. [67], the reserve joint torques should be smaller than 5 % of the net joint moments and the residual moments should be smaller than 1 % of the centre of mass height times the magnitude of the net external force. The residuals in the present models are currently higher than that, with absolute maximum values of 200 Nm for hip flexion moment, 150 Nm for hip adduction moment and 50 Nm for internal hip rotation moment during the analysed running stance phase.

The high magnitudes of actuators in the present musculoskeletal models could cause non-realistic outcome of the analysis because of exclusion or alteration of contributions from computed muscle forces. Future work will aim at identifying the reason for the high residuals and attempt to reduce them. By minimizing the obtained residuals, an accurate representation of physical phenomena can be validated, thereby ensure trustworthy conclusions based on the computed musculoskeletal simulations [67].

5.2 The Finite Element Model

This section presents the biomechanical outcomes of the FE models grouped by variable of interest. For each outcome, results obtained during walking are presented first followed by those during running to facilitate direct comparison across locomotion modes.

5.2.1 Contact Stresses in the Cartilage

Prediction of stress distribution within the acetabular cartilage is often evaluated during walking [4], [5], [6], [21], [27], [68]. Harris et al. investigated cartilage contact stresses in ten participants across three activities, among those was walking. The study assessed thereby variations in contact stresses and areas among subjects and across loading scenarios using FE analysis. Xiong et al. included two participants in a similar framework to the present study with integrated motion capture data of walking, musculoskeletal modelling and FE analysis with subject-specific geometry to investigate changes in contact stress throughout the gait cycle. In the present FE models, the maximum von Mises stress during walking occurred at approximately 10 % of the stance phase (Figure 4.6), in correspondence to the first and highest peak in the ground reaction force (Figure 4.2). Slightly higher stress magnitudes were observed in the present study during walking compared to Harris et al. and Xiong et al. [5], [68]. The upper range of stress magnitudes reported by Harris et al. were 9 MPa throughout walking stance, leading to 22 % higher magnitudes found in the present study [5]. A more pronounced difference in magnitude of 57 % was found compared to Xiong et al. [68]. The high magnitudes for the simulated stance phase of walking might be driven by the substantial high peak in joint reaction force (Figure 4.3) corresponding to the first peak in ground reaction force. However, from mid-stance to toe-off phase, the stress magnitudes reported in the present study in Figure 4.6 (2-9 MPa) are comparable to the values reported by Harris et al. and Xiong et al. of 7.5 MPa and 7 MPa, respectively.

The acetabular cartilage stress distribution areas for walking shown in Figure 4.8 demonstrated good agreement with those reported by Harris et al. (Figure 5.6), particularly for subject 7-10, where the highest magnitudes were observed in the superior-posterior, superior-anterior and inferior-anterior regions of the cartilage [5].

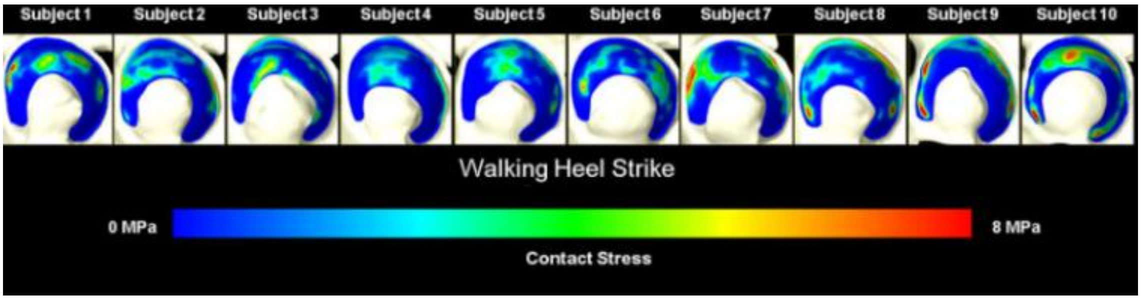

Figure 5.6: Contact stresses in the acetabular cartilage for each subject during walking heel strike. Adapted from [5].

When comparing ground reaction forces between walking and running, significantly higher magnitudes are observed during running (Figure 5.1). The ground reaction force peak during walking is approximately 1-1.4 BW, while running exhibits a loading peak at approximately 2-2.5 BW [62]. Consequently, a direct comparison between the present running simulation and previously published walking studies would not fully reflect the relative mechanical loading of the hip joint. Since finite element studies investigating acetabular cartilage loading during running are limited, an assumption was made to enable comparison between walking and running simulations. Based on the increased ground reaction force during running, it was hypothesized that cartilage stresses would be approximately twice as high during running compared to walking. This assumption should be interpreted with caution, since several nonlinearities are present in the pipeline, including the FE model using a nonlinear hyperelastic material model for the acetabular cartilage.

During running, the maximum von Mises stress in the cartilage occurred at mid-stance shown in Figure 4.5 at the time point corresponding to the second loading peak in ground reaction force during stance in running shown in Figure 4.2. Similarly to walking, the stress distribution areas within the acetabular cartilage during running (Figure 4.7) exhibited similar distributions to those reported by Harris et al. in subject 7-10 (Figure 5.6), where the highest magnitudes occurred in the superior-posterior, superior-anterior and inferior-anterior regions of the cartilage [5]. Considering the mentioned assumption for running, the cartilage stress peak of 13.5 MPa predicted in the present study is comparable to the approximately 14 MPa reported by Harris et al. Furthermore, the predicted stress magnitudes throughout the running stance phase remained consistent within the a similar range to those reported by Harris et al. when accounting for the assumption [5]. The peak in stress observed at 10 % of stance, approximately 13 MPa, is also comparable to the magnitudes reported by Xiong et al. for walking at a similar magnitude of 14 MPa when applying the assumption [68].

Compared to the reported results for walking in the present study, running resulted in 18.5 % higher peak contact stresses, while stress concentrations remained located in similar regions including the superior-posterior, superior-anterior and inferior-anterior areas of the cartilage. Excluding the relatively high stress concentration associated with the first ground reaction force peak in walking, running produced approximately 33 % higher peak contact stresses compared to those observed during walking.

5.2.2 Contact Pressure in the Cartilage

Anderson et al. have developed a FE model of the hip joint to predict cartilage contact stress with subject-specific geometry using in vivo loads measured during walking and assess sensitivity of model predictions to geometry, boundary conditions and material properties [4]. The contact pressure during walking in the present study (Figure 4.10) did not demonstrate agreement with the magnitudes reported by Anderson et al. For walking, a more pronounced difference was observed of 70 % greater than the reported values by Anderson et al. [4]. The difference might be driven by the high joint reaction forces corresponding to the first peak in ground reaction force, where the highest contact pressure occurs. In a separate study, Anderson et al. used the previous published study as a basis to vary degrees of simplified geometry along with using a model with rigid bone material assumption. Effects on predictions of cartilage stress in, among other activities, walking were thereby investigated by Anderson et al. In this study by Anderson et al., the contact pressure for the rigid bone model was 50 % lower compared to the values reported for walking in the present study [27].

Similarly to walking in the present study, the contact pressure during running (Figure 4.9) did not demonstrate agreement with the magnitudes reported by Anderson et al. The cartilage contact pressure peak of 33.7 MPa predicted in the present study was approximately 50 % greater than the magnitudes reported for walking by Anderson et al. when applying the earlier discussed assumption [4]. However, in the subsequent study by Anderson et al. the contact pressure distributions within the acetabular cartilage were comparable to those predicted in the present study. Furthermore, the peak contact pressure of 33.7 MPa was comparable to the 30 MPa reported by Anderson et al. when applying the assumption regarding load magnitudes in running [27]. The variability in contact pressure between the two studies by Anderson et al. might have resulted from geometric simplifications, material properties and boundary conditions.

5.2.3 Contact Area

The fluctuations in contact area for walking and running observed in Figure 4.11 appeared to be consistent with the oscillations in joint reaction force shown in Figure 4.3, suggesting that variations in force magnitude potentially affects the progression of contact area throughout the stance phase. For walking, the reduction in contact area might as the stance phase progresses be explained by the sliding of the acetabular cartilage towards toe-off, which was indicated by the contact progression observed in the FE simulation. The relatively stable contact area of approximately 430 mm^2 is consistent with the range reported for both models in a study by Xiong et al. with contact areas between 316.7-787.6 mm^2 and 293.6-998.4 mm^2 respectively [68]. However, a study by Anderson et al. reported a significantly narrower range in contact area of 304.2-366.1 mm^2, which only was comparable to the contact area at toe-off [4].

Similarly to walking, running was associated with a reduction in contact area as the stance phase progresses, suggesting sliding of the cartilage towards toe-off. This was also indicated by the contact progression observed in the FE simulation. Additionally, the relatively stable contact area of approximately 530 mm^2 for running is consistent with the ranges reported in the study by Xiong et al. [68]. This contact area is also comparable to the one reported by Harris et al. of approximately 600 mm^2 throughout walking stance [5]. However, a greater reduction in contact area during running (494 mm^2) was observed from mid-stance to toe-off phase compared to walking (130 mm^2). This may indicate that the contact area undergoes a larger displacement during running, which could be associated with greater range of motion and increased sliding of the cartilage than during walking.

5.2.4 Hip Joint Moments

Moment-driven FE simulations failed to converge beyond the first peak in ground reaction force for walking and beyond mid-stance for running, suggesting that these time points caused convergence difficulties. For walking, a peak in the x (medial-lateral) moment component at -225 Nm and the y (anterior-posterior) moment component at -140 Nm (Figure 4.4) were observed at the time point between the initial heel strike and the first peak in ground reaction force. Similarly, for running, a significantly high peak in the x (medial-lateral) moment component at 37 Nm from the outcome of the joint reaction load analysis (Figure 4.4) was observed, while the other moment components remained relatively stable at ± 7 Nm and ± 10 Nm respectively. Those peaks in both walking and running occurred in correspondence to peaks in joint reaction force and von Mises stress, which together potentially contribute to convergence difficulties. The peak in moment may be influenced by artefacts in the input data during the joint reaction analysis. Thus, a FE model including moments instead of rotations could not simulated in this pipeline for neither walking nor running and was thereby excluded in the pipeline.

5.2.5 Material Model of Cartilage

Although cartilage exhibits a biphasic behaviour, an incompressible neo-Hookean hyperelastic material model was used to model articular cartilage in the present FE model. A material model with higher complexity may provide a more physiologically realistic representation of the cartilage behaviour and predict different observations of the behaviour, i.e. long-term loading effects and time-dependent fluid flow [25]. The contact pressure within the articular cartilage would additionally be influenced by including a more complex material model [26]. However, a complex material model requires more incorporated material coefficients, increasing the number of unknowns needed to be determined and thereby complicates parameter identification from experimental data [25]. Additionally, complex material models are substantially more computationally demanding. However, hyperelastic material models have shown comparable computational stress predictions during instantaneous loading to ones with higher complexity [4], [5], [26]. The assumption of incompressibility is supported by in vitro studies, suggesting minimal fluid flow during instantaneous loading, which is simulated in this pipeline [4]. Since predictions of cartilage contact stress and contact area are relatively insensitive to constitutive model descriptions, simpler material models, including a hyperelastic model, have been shown to predict these parameters accurately [25]. Thus, this master's thesis leaves the investigation of the most appropriate material model to future studies. The results in the present study can be interpreted as an ideal foundation for this by allowing construction of a FE model with subject-specific boundary conditions from gait data for both walking and running.

5.3 Limitations

This master's thesis developed a pipeline that connects musculoskeletal and finite element modelling to investigate load predictions within the hip joint. However, the pipeline in its present form exhibits some limitations.

One limitation is that the pipeline has been developed and tested on one single subject and one single gait cycle of a 30-second-long trial for walking respectively running were analysed. Since variability between subjects was not evaluated in the present study, the reported results should be interpreted with caution and might not be representative for a broader population. However, this work represents, to the best of knowledge, one of the first implementations of an integrated musculoskeletal and finite element modelling pipeline, and it is indeed opening up the possibility to investigate inter- and intra-subject variability in future investigations. Data for more subjects is already available for that, thus allowing to assess the variability between subjects and gait cycles for the same subject. This might improve the accuracy of the results and enable a more robust assessment of potential artefacts in the pipeline for the musculoskeletal modelling analyses.

Another limitation is that the outputs from the musculoskeletal modelling were not ideal. Oscillations in the computed joint reaction forces and large transient peaks in joint reaction moment were observed for both walking and running (Figure 4.3 and 4.4). Combined with residual forces outside the margins stated by Hicks et al. in the musculoskeletal simulations suggests that improvements are needed for the methodology of the musculoskeletal analyses, particularly in the static optimization and joint reaction analysis [67]. The computed kinematics appeared smooth and physiologically realistic when compared to literature [63], [64], whereas oscillations emerged after the static optimization and joint reaction analysis. Similar findings regarding high residuals were reported by Flahaut, who identified large transient spike using the same motion capture data used in the present study. The spikes particularly occurred during stance phase of running with a variability in peaks near the initial contact. These inconsistencies likely arise from measurement noise, soft tissue artefacts, model scaling procedures and deviations between kinematics, ground reaction force and inverse dynamics solutions. Flahaut reported that minor variability between kinematics and ground reaction force measurements may generate significant vertical residuals, which in turn is sensitive to artefacts in treadmill dynamics, segmental kinematics and ground reaction force measurements [54]. This might explain the observed oscillations in the hip joint reaction force and moments shown in Figure 4.3 and 4.4. Additionally, Flahaut observed that limitations in accurately capturing vertical loading dynamics may cause the large vertical residuals [54]. The uncertainty in the produced joint contact forces reflected in an uncertainty about the output of the FE models, which used those contact forces as input. A mesh convergence analysis was not performed in the pipeline, making it difficult to ensure accuracy and independency of mesh size. Thus, it could not be confirmed whether the same results were obtained using a finer mesh size compared to a coarser one. Nevertheless, the FE simulations were able to successfully converge and produce physiologically reasonable results in terms of stress state in the cartilage, at least when combining joint reaction forces and the computed kinematics for the rotations as boundary conditions. This suggests that the developed pipeline is robust, although validation and refinement of the musculoskeletal modelling pipeline are needed. Future studies should focus on minimizing the residuals and conduct a mesh convergence analysis to improve the outcomes of the musculoskeletal modelling part.

Additionally, the present study analysed cartilage contact mechanics in young populations. Osteoarthritis is more prevalent in middle-aged and elderly populations. The reported results in both stress magnitude and spatial distribution within the articular cartilage should therefore be interpreted with caution in a direct comparison between these populations, particularly between young and elderly individuals. Age-related changes in joint biomechanics and physical function, including thinner cartilage that may be associated with higher stress within the joint, may alter contact mechanics through distribution and loading patterns, thereby limiting direct comparison of outcomes across age groups.

An additional limitation is that no CT or MRI images were available of the analysed subject in this master's thesis. Harris et al. have reported that subject-specific joint geometry produces substantial variation in contact stress distribution within the articular cartilage with greater differences observed among subjects than across loading activities within an individual subject. Variations in joint geometry also influenced the contact patterns and the location of peak contact stress, potentially causing discontinuities in stress distribution within the cartilage. Consequently, a substantially reduced magnitude in contact stress and a more uniform contact distribution were found in FE models with ideal joint geometry [5]. Additionally, a simplified joint geometry may lack the details needed to accurately capture physiologically realistic predictions of cartilage contact pressure. Since minor differences in geometry can cause large variability in contact mechanics, subject-specific joint geometry can substantially improve the prediction accuracy [27]. Thus, inclusion of subject-specific joint geometry of the analysed subject would improve the prediction accuracy within the acetabular cartilage. Since a generic hip joint geometry was used in the present FE model, the reported results should be interpreted as providing predictions of magnitude and spatial distribution of cartilage contact mechanics rather than exact subject-specific estimations.

5.4 Future Improvements

In future studies, the prescribed rotations in the present FE model could be replaced by joint reaction moments in the corresponding directions. Currently, the prescribed rotations mimic the experimental motion capture data extracted from the musculoskeletal modelling, while the joint reaction moments predicted by the FE model are not equivalent to those computed in the musculoskeletal procedure. However, the movement in the FE simulation might differ due to inconsistencies in the input data for the analysis. Moments and rotations are intrinsically connected to each other, where computed moments should correspond to computed kinematics. Thus, smooth and physiologically realistic kinematics should result in comparably smooth hip joint moments [69]. Future studies should focus on minimizing differences between computed moments and kinematics boundary conditions to enable a representative implementation of joint reaction moments in the FE model.

Based on the developed functional pipeline, inclusion of more participants and thereby increasing the number of analysed gait cycles would improve the generalisability and the overall scientific impact of the results. The assessment of load predictions may strengthen conclusions regarding variability between subjects and help characterize prediction of load magnitude and spatial distribution. Consequently, the predictions would become more representative for a broader population. Improved characterization of joint reaction loads is crucial because they influence cartilage mechanics and may contribute to progression of osteoarthritis. More reliable load predictions might improve biomechanical assessment tools to enable identification of biomechanical factors associated with cartilage degeneration.

Future applications would also benefit from a more automated pipeline, especially when having future clinical application as a target. Technical knowledge is often limited among nursing professionals where an automated pipeline would facilitate usage. Additionally, the time needed for using the clinical application could be reduced through increased automation, which would be beneficial in terms of the high clinical workflow.

5.5 Ethics

All subjects included in the provided experimental data read and signed a letter of informed consent approved by the local Ethics Review Authority [54]. The shared experimental data was anonymized before being provided to the author of this thesis and all data were stored according to GDPR requirements. No additional CT or MRI images were available corresponding to the subjects, thereby avoiding any further exposure to radiation.

The FE hip joint model was based on a generic geometry obtained from an open-access resource. Moshfeghifar et al. generated the geometry using previously acquired clinical images, avoiding need for custom image acquisition associated with risk of radiation exposure. Furthermore, the study also followed the FAIR principles for open-access FE models [56]. The usage of a generic geometry eliminated the need to acquire subject-specific CT or MRI images for the present study and therefore imposed no additional burden on the subjects. Additionally, all analyses were conducted using previously collected data. Thus, subject anonymity was maintained throughout the master's thesis.

From a clinical perspective, ethical considerations should encompass the entire workflow of the developed pipeline to generate subject-specific cartilage stress distributions within the hip joint. The functional pipeline requires imaging data, i.e. CT or MRI images, to reconstruct a patient-specific geometry of the hip joint. While MRI does not involve radiation, CT imaging would expose patients to radiation. Additionally, informed consent is also required for each patient to enable collection of motion capture data, which provide subject-specific loading inputs for the FE models. Since both the imaging data and collection of motion capture data constitute sensitive personal data, the data must be stored, processed and shared in accordance with GDPR. Therefore, clinical applications of the pipeline require balancing the potential benefits of personalized biomechanical assessment against patient burden, radiation exposure and the risks to patient privacy.

6 Conclusion

During this master's thesis, a pipeline has been developed to investigate stress distributions within the hip joint during walking and running. Joint reaction forces acting within the hip were extracted from musculoskeletal modelling analyses along with hip joint kinematics. The extracted forces and kinematics were subsequently implemented into a finite element hip joint model to represent subject-specific loading during the simulated stance phase for the respective gait. Thus, the pipeline enables evaluation of stress distributions in the acetabular cartilage accounting for subject-specific loading.

The pipeline successfully integrated motion capture data, musculoskeletal modelling and finite element modelling to enable stress evaluation within the acetabular cartilage using subject-specific loading. Subject-specific loading allows a more subject-specific representation of loading during evaluation of cartilage stress to potentially support early detection and treatment of osteoarthritis in the future. The workflow provides physiologically realistic results that were generally consistent with literature. This indicates that the integrated modelling framework provides a feasible approach for investigating cartilage loading during both walking and running.

Finally, the pipeline bridges experimental movement analysis and tissue-level mechanics, enabling improved understanding of mechanical factors that may contribute to progression of osteoarthritis. Thus, the integrated framework contributes to a more personalized biomechanical assessment tool rather than generic loading assumptions. The pipeline provides a platform for testing the hypothesis that cartilage stress magnitudes vary throughout progression of osteoarthritis, which might enable easier distinction between healthy and pathological joints. Future research can build upon this pipeline for translating subject-specific motion capture data into cartilage-level stress distributions through an integrated modelling framework.

7 References

[1] H. A. Wieland, M. Michaelis, B. J. Kirschbaum, and K. A. Rudolphi, ‘Osteoarthritis — an untreatable disease?’, *Nat Rev Drug Discov*, vol. 4, no. 4, pp. 331–344, Apr. 2005, doi: 10.1038/nrd1693.

[2] World Health Organization, ‘Osteoarthritis’, World Health Organization. [Online]. Available: https://www.who.int/news-room/fact-sheets/detail/osteoarthritis/

[3] D. E. Lunn, A. Lampropoulos, and T. D. Stewart, ‘Basic biomechanics of the hip’, *Orthopaedics and Trauma*, vol. 30, no. 3, pp. 239–246, Jun. 2016, doi: 10.1016/j.mporth.2016.04.014.

[4] A. E. Anderson, B. J. Ellis, S. A. Maas, C. L. Peters, and J. A. Weiss, ‘Validation of Finite Element Predictions of Cartilage Contact Pressure in the Human Hip Joint’, *Journal of Biomechanical Engineering*, vol. 130, no. 5, p. 051008, Oct. 2008, doi: 10.1115/1.2953472.

[5] M. D. Harris, A. E. Anderson, C. R. Henak, B. J. Ellis, C. L. Peters, and J. A. Weiss, ‘Finite element prediction of cartilage contact stresses in normal human hips’, *Journal Orthopaedic Research*, vol. 30, no. 7, pp. 1133–1139, Jul. 2012, doi: 10.1002/jor.22040.

[6] J. Li, ‘Development and validation of a finite-element musculoskeletal model incorporating a deformable contact model of the hip joint during gait’, *Journal of the Mechanical Behavior of Biomedical Materials*, 2021.

[7] A. D. Sylvester, S. G. Lautzenheiser, and P. A. Kramer, ‘A review of musculoskeletal modelling of human locomotion’, *Interface Focus.*, vol. 11, no. 5, p. 20200060, Oct. 2021, doi: 10.1098/rsfs.2020.0060.

[8] S. L. Delp *et al.*, ‘OpenSim: Open-Source Software to Create and Analyze Dynamic Simulations of Movement’, *IEEE Trans. Biomed. Eng.*, vol. 54, no. 11, pp. 1940–1950, Nov. 2007, doi: 10.1109/TBME.2007.901024.

[9] H.-H. Wu, D. Wang, A.-B. Ma, and D.-Y. Gu, ‘Hip joint geometry effects on cartilage contact stresses during a gait cycle’, in *2016 38th Annual International Conference of the IEEE Engineering in Medicine and Biology Society (EMBC)*, Orlando, FL, USA: IEEE, Aug. 2016, pp. 6038–6041. doi: 10.1109/EMBC.2016.7592105.

[10] N. Saabye Ottosen and H. Petersson, *Introduction to the finite element method*. Edinburgh Gate: Pearson Education Limited, 1992.

[11] A. Esrafilian *et al.*, ‘An EMG-Assisted Muscle-Force Driven Finite Element Analysis Pipeline to Investigate Joint- and Tissue-Level Mechanical Responses in Functional Activities: Towards a Rapid Assessment Toolbox’, *IEEE Trans. Biomed. Eng.*, vol. 69, no. 9, pp. 2860–2871, Sep. 2022, doi: 10.1109/TBME.2022.3156018.

[12] D. P. Byrne, K. J. Mulhall, and J. F. Baker, ‘Anatomy & Biomechanics of the Hip’, *TOSMJ*, vol. 4, no. 1, pp. 51–57, Jan. 2010, doi: 10.2174/1874387001004010051.

[13] A. Zaghloul, ‘Hip Joint: Embryology, Anatomy and Biomechanics’, *BJSTR*, vol. 12, no. 3, Dec. 2018, doi: 10.26717/BJSTR.2018.12.002267.
[14] V. Mahadevan, ‘Anatomy of the pelvis’, *Surgery (Oxford)*, vol. 36, no. 7, pp. 333–338, Jul. 2018, doi: 10.1016/j.mpsur.2018.04.005.
[15] A. Chang, G. Breeland, A. C. Black, and J. B. Hubbard, *Anatomy, Bony Pelvis and Lower Limb: Femur*, StatPearls. Treasure Island (FL): StatPearls Publishing, 2023. [Online]. Available: https://www.ncbi.nlm.nih.gov/books/NBK532982/
[16] K. Arunkumar, U. Delhiraj, and S. S. Kumar, ‘Morphologic and Morphometric Study of Human Acetabulum and its Clinical Significance’, *JCDR*, 2021, doi: 10.7860/JCDR/2021/46566.14556.
[17] *Servier Medical Art provided by Servier, licensed under a Creative Commons Attribution 3.0 unported license*. [Online]. Available: https://smart.servier.com/
[18] E. Dall’Ara and V. S. Cheong, ‘Bone biomechanics’, in *Human Orthopaedic Biomechanics*, Elsevier, 2022, pp. 97–120. doi: 10.1016/B978-0-12-824481-4.00007-X.
[19] F. Johannesdottir, S. R. Emerzian, and M. L. Bouxsein, ‘Bone structure and biomechanics’, in *Encyclopedia of Endocrine Diseases*, Elsevier, 2026, pp. 538–551. doi: 10.1016/B978-0-443-13825-6.00030-3.
[20] P. Bazyar, A. Baumgart, H. Altenbach, and A. Usbeck, ‘An Overview of Selected Material Properties in Finite Element Modeling of the Human Femur’, *Biomechanics*, vol. 3, no. 1, pp. 124–135, Mar. 2023, doi: 10.3390/biomechanics3010012.
[21] M. Li *et al.*, ‘Discrete element and finite element methods provide similar estimations for hip joint contact mechanics during walking gait’, *Journal of Biomechanics*, vol. 115, p. 110163, Jan. 2021, doi: 10.1016/j.jbiomech.2020.110163.
[22] Z. Zou, A. Chávez-Arreola, P. Mandal, T. N. Board, and T. Alonso-Rasgado, ‘Optimization of the position of the acetabulum in a ganz periacetabular osteotomy by finite element analysis’, *Journal Orthopaedic Research*, vol. 31, no. 3, pp. 472–479, Mar. 2013, doi: 10.1002/jor.22245.
[23] J. M. Mansour, ‘Biomechanics of Cartilage’, 2021. doi: 10.3390/life11040302.
[24] A. J. Sophia Fox, A. Bedi, and S. A. Rodeo, ‘The Basic Science of Articular Cartilage: Structure, Composition, and Function’, *Sports Health: A Multidisciplinary Approach*, vol. 1, no. 6, pp. 461–468, Nov. 2009, doi: 10.1177/1941738109350438.
[25] C. R. Henak, A. E. Anderson, and J. A. Weiss, ‘Subject-Specific Analysis of Joint Contact Mechanics: Application to the Study of Osteoarthritis and Surgical Planning’, *Journal of Biomechanical Engineering*, vol. 135, no. 2, p. 021003, Feb. 2013, doi: 10.1115/1.4023386.
[26] X. Hua, J. Li, E. De Pieri, and S. J. Ferguson, ‘Multiscale biomechanics of the biphasic articular cartilage in the natural hip joint during routine

activities', *Computer Methods and Programs in Biomedicine*, vol. 215, p. 106606, Mar. 2022, doi: 10.1016/j.cmpb.2021.106606.
[27] A. E. Anderson, B. J. Ellis, S. A. Maas, and J. A. Weiss, 'Effects of idealized joint geometry on finite element predictions of cartilage contact stresses in the hip', *Journal of Biomechanics*, vol. 43, no. 7, pp. 1351–1357, May 2010, doi: 10.1016/j.jbiomech.2010.01.010.
[28] J. Bergström, 'Elasticity/Hyperelasticity', in *Mechanics of Solid Polymers*, Elsevier, 2015, pp. 209–307. doi: 10.1016/B978-0-323-31150-2.00005-4.
[29] N. Saabye Ottosen and M. Ristinmaa, *The Mechanics of Constitutive Modeling*, vol. 2005. doi: https://doi.org/10.1016/B978-0-08-044606-6.X5000-0.
[30] R. M. Hackett, *Hyperelasticity Primer*. Cham: Springer International Publishing, 2018. doi: 10.1007/978-3-319-73201-5.
[31] M. Shahzad, A. Kamran, M. Z. Siddiqui, and M. Farhan, 'Mechanical Characterization and FE Modelling of a Hyperelastic Material', *Mat. Res.*, vol. 18, no. 5, pp. 918–924, Oct. 2015, doi: 10.1590/1516-1439.320414.
[32] Dassault Systèmes®, '22.5.1 Hyperelastic behavior of rubberlike materials', Abaqus Documentation. [Online]. Available: http://130.149.89.49:2080/v2016/books/usb/default.htm?startat=pt05ch22s05abm07.html#usb-mat-chyperelastic
[33] K. C. G. Ng, J. R. T. Jeffers, and P. E. Beaulé, 'Hip Joint Capsular Anatomy, Mechanics, and Surgical Management', *The Journal of Bone and Joint Surgery*, vol. 101, no. 23, pp. 2141–2151, Dec. 2019, doi: 10.2106/JBJS.19.00346.
[34] J. D. Hewitt, R. R. Glisson, F. Guilak, and T. P. Vail, 'The mechanical properties of the human hip capsule ligaments', *The Journal of Arthroplasty*, vol. 17, no. 1, pp. 82–89, Jan. 2002, doi: 10.1054/arth.2002.27674.
[35] M. C. Gash, P. F. Kandle, I. V. Murray, and M. A. Varacallo, *Physiology, Muscle Contraction*, StatPearls. Treasure Island (FL): StatPearls Publishing, 2023. [Online]. Available: https://www.ncbi.nlm.nih.gov/sites/books/NBK537140/
[36] H. J. Freund, 'Motor unit and muscle activity in voluntary motor control.', *Physiological Reviews*, vol. 63, no. 2, pp. 387–436, Apr. 1983, doi: 10.1152/physrev.1983.63.2.387.
[37] R. G. Ellis, B. J. Sumner, and R. Kram, 'Muscle contributions to propulsion and braking during walking and running: Insight from external force perturbations', *Gait & Posture*, vol. 40, no. 4, pp. 594–599, Sep. 2014, doi: 10.1016/j.gaitpost.2014.07.002.
[38] K. Sasaki and R. R. Neptune, 'Differences in muscle function during walking and running at the same speed', *Journal of Biomechanics*, vol. 39, no. 11, pp. 2005–2013, 2006, doi: 10.1016/j.jbiomech.2005.06.019.
[39] S. R. Hamner, A. Seth, and S. L. Delp, 'Muscle contributions to propulsion and support during running', *Journal of Biomechanics*, vol. 43, no. 14, pp. 2709–2716, Oct. 2010, doi: 10.1016/j.jbiomech.2010.06.025.

[40] D. E. Lieberman, D. A. Raichlen, H. Pontzer, D. M. Bramble, and E. Cutright-Smith, ‘The human gluteus maximus and its role in running’, *Journal of Experimental Biology*, vol. 209, no. 11, pp. 2143–2155, Jun. 2006, doi: 10.1242/jeb.02255.
[41] J. Afonso *et al.*, ‘The Hamstrings: Anatomic and Physiologic Variations and Their Potential Relationships With Injury Risk’, *Front. Physiol.*, vol. 12, p. 694604, Jul. 2021, doi: 10.3389/fphys.2021.694604.
[42] J. M. Wakeling, M. Febrer-Nafría, and F. De Groote, ‘A review of the efforts to develop muscle and musculoskeletal models for biomechanics in the last 50 years’, *Journal of Biomechanics*, vol. 155, p. 111657, Jun. 2023, doi: 10.1016/j.jbiomech.2023.111657.
[43] M. R. Allen and J. Wallace, *Skeletal Tissue Mechanics*. Cham: Springer Nature Switzerland, 2025. doi: 10.1007/978-3-031-90609-1.
[44] M. S. Harrington, S. D. F. Di Leo, C. A. Hlady, and T. A. Burkhart, ‘Musculoskeletal modeling and movement simulation for structural hip disorder research: A scoping review of methods, validation, and applications’, *Heliyon*, vol. 10, no. 15, p. e35007, Aug. 2024, doi: 10.1016/j.heliyon.2024.e35007.
[45] Y. Gao *et al.*, ‘Effect of Hip Joint Center on MULTI-BODY Dynamics and Contact Mechanics of Hip Arthroplasty for Crowe IV Dysplasia’, *Orthopaedic Surgery*, vol. 14, no. 11, pp. 3061–3069, Nov. 2022, doi: 10.1111/os.13272.
[46] S. Jahangir *et al.*, ‘Effect of uncertainties in musculoskeletal modeling inputs on sensitivity of knee joint finite element simulations’, *Med. Eng. Phys.*, vol. 138, no. 1, p. 104313, Apr. 2025, doi: 10.1016/j.medengphy.2025.104313.
[47] M. DeMers, ‘Webinar: Estimating Joint Loads in OpenSim’. Accessed: Jan. 29, 2026. [Online]. Available: https://www.youtube.com/watch?v=ly4rhOOifO0
[48] J. L. Hicks, *How Inverse Kinematics Works*. (Jul. 05, 2018). [Online]. Available: https://opensimconfluence.atlassian.net/wiki/spaces/OpenSim/pages/53090047/How+Inverse+Kinematics+Works
[49] J. L. Hicks, *How Static Optimization Works*. (Jul. 05, 2018). [Online]. Available: https://opensimconfluence.atlassian.net/wiki/spaces/OpenSim/pages/53089619/How+Static+Optimization+Works
[50] K. M. Steele, M. S. DeMers, M. H. Schwartz, and S. L. Delp, ‘Compressive tibiofemoral force during crouch gait’, *Gait & Posture*, vol. 35, no. 4, pp. 556–560, Apr. 2012, doi: 10.1016/j.gaitpost.2011.11.023.
[51] A. Seth *et al.*, ‘OpenSim: Simulating musculoskeletal dynamics and neuromuscular control to study human and animal movement’, *PLoS Comput Biol*, vol. 14, no. 7, p. e1006223, Jul. 2018, doi: 10.1371/journal.pcbi.1006223.

[52] Dassault Systémes®, *Abaqus Unified FEA- SIMULIA™*. [Online]. Available: https://www.3ds.com/products/simulia
[53] A. Ramos and J. A. Simões, 'Tetrahedral versus hexahedral finite elements in numerical modelling of the proximal femur', *Med. Eng. Phys.*, vol. 28, no. 9, pp. 916–924, Nov. 2006, doi: 10.1016/j.medengphy.2005.12.006.
[54] Z. Flahaut, 'Neuromuscular responses and cost of transport across increasing physiological strain during fatigued running in young adults', *Université d'Ottawa / University of Ottawa*, May 2026, doi: https://doi.org/10.20381/ruor-31975.
[55] D. S. Catelli, M. Wesseling, I. Jonkers, and M. Lamontagne, 'A musculoskeletal model customized for squatting task', *Computer Methods in Biomechanics and Biomedical Engineering*, vol. 22, no. 1, pp. 21–24, Jan. 2019, doi: 10.1080/10255842.2018.1523396.
[56] F. Moshfeghifar *et al.*, 'LibHip: An open-access hip joint model repository suitable for finite element method simulation', *Computer Methods and Programs in Biomedicine*, vol. 226, p. 107140, Nov. 2022, doi: 10.1016/j.cmpb.2022.107140.
[57] M. Akrami, K. Craig, M. Dibaj, A. A. Javadi, and A. Benattayallah, 'A three-dimensional finite element analysis of the human hip', *Journal of Medical Engineering & Technology*, vol. 42, no. 7, pp. 546–552, Oct. 2018, doi: 10.1080/03091902.2019.1576795.
[58] C. L. Abraham, S. A. Maas, J. A. Weiss, B. J. Ellis, C. L. Peters, and A. E. Anderson, 'A new discrete element analysis method for predicting hip joint contact stresses', *Journal of Biomechanics*, vol. 46, no. 6, pp. 1121–1127, Apr. 2013, doi: 10.1016/j.jbiomech.2013.01.012.
[59] A. Kewley, J. Van Beesel, and A. Seth, 'OpenSim Creator: An Interactive User Interface for Building OpenSim Musculoskeletal Models', *JOSS*, vol. 11, no. 117, p. 8284, Jan. 2026, doi: 10.21105/joss.08284.
[60] D. Girardeau-Montaut, *CloudCompare- open source project*. [Online]. Available: https://www.cloudcompare.org/
[61] G. Giarmatzis, I. Jonkers, M. Wesseling, S. Van Rossom, and S. Verschueren, 'Loading of Hip Measured by Hip Contact Forces at Different Speeds of Walking and Running', *Journal of Bone and Mineral Research*, vol. 30, no. 8, pp. 1431–1440, Aug. 2015, doi: 10.1002/jbmr.2483.
[62] T. K. Uchida and S. Delp, *Biomechanics of movement: the science of sports, robotics, and rehabilitation*. Cambridge: The MIT press, 2020.
[63] D. Chandra, N. D. Anggraeni, T. Dirgantara, S. Mihradi, and A. I. Mahyuddin, 'Improvement of Three-dimensional Motion Analyzer System for the Development of Indonesian Gait Database', *Procedia Manufacturing*, vol. 2, pp. 268–274, 2015, doi: 10.1016/j.promfg.2015.07.047.
[64] A. G. Schache, P. D. Blanch, D. A. Rath, T. V. Wrigley, R. Starr, and K. L. Bennell, 'A comparison of overground and treadmill running for measuring the three-dimensional kinematics of the lumbo–pelvic–hip complex',

Clinical Biomechanics, vol. 16, no. 8, pp. 667–680, Oct. 2001, doi: 10.1016/S0268-0033(01)00061-4.
[65] E. Passmore, H. K. Graham, and M. Sangeux, 'Defining the medial-lateral axis of the femur: Medical imaging, conventional and functional calibration methods lead to differences in hip rotation kinematics for children with torsional deformities', *Journal of Biomechanics*, vol. 69, pp. 156–163, Mar. 2018, doi: 10.1016/j.jbiomech.2018.01.018.
[66] G. Bergmann, F. Graichen, and A. Rohlmann, 'Hip joint loading during walking and running, measured in two patients', *Journal of Biomechanics*, vol. 26, no. 8, pp. 969–990, Aug. 1993, doi: 10.1016/0021-9290(93)90058-M.
[67] J. L. Hicks, T. K. Uchida, A. Seth, A. Rajagopal, and S. L. Delp, 'Is My Model Good Enough? Best Practices for Verification and Validation of Musculoskeletal Models and Simulations of Movement', *Journal of Biomechanical Engineering*, vol. 137, no. 2, p. 020905, Feb. 2015, doi: 10.1115/1.4029304.
[68] B. Xiong *et al.*, 'Changes in hip joint contact stress during a gait cycle based on the individualized modeling method of "gait-musculoskeletal system-finite element"', *J Orthop Surg Res*, vol. 17, no. 1, p. 267, Dec. 2022, doi: 10.1186/s13018-022-03094-5.
[69] B. Musa, J. Chen, G. Martin, K. H. Lostroscio, and A. Peebles, 'A Comparative Study of Lower-Limb Joint Angles and Moment Estimations Across Different Gait Conditions Using OpenSim for Body-Weight Offloading Applications', *Biomechanics*, vol. 6, no. 1, p. 27, Mar. 2026, doi: 10.3390/biomechanics6010027.

8 Appendix

The spatial strain field distribution for running and walking are visualized in Supplementary Figure 8.1 and Supplementary Figure 8.2, respectively.

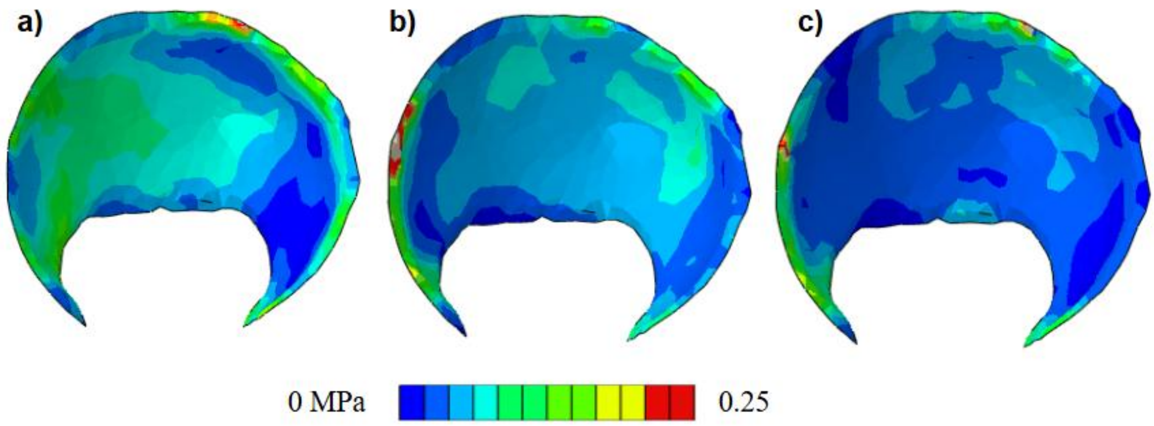

Figure 8.1: The load distribution of the maximum principal strain in the acetabular cartilage during running stance at a) the first peak of the ground reaction force (10 % of the stance phase), b) the second peak in the ground reaction force (44 % of the stance phase) and c) the strain at the maximum von Mises stress (50 % of the stance phase).

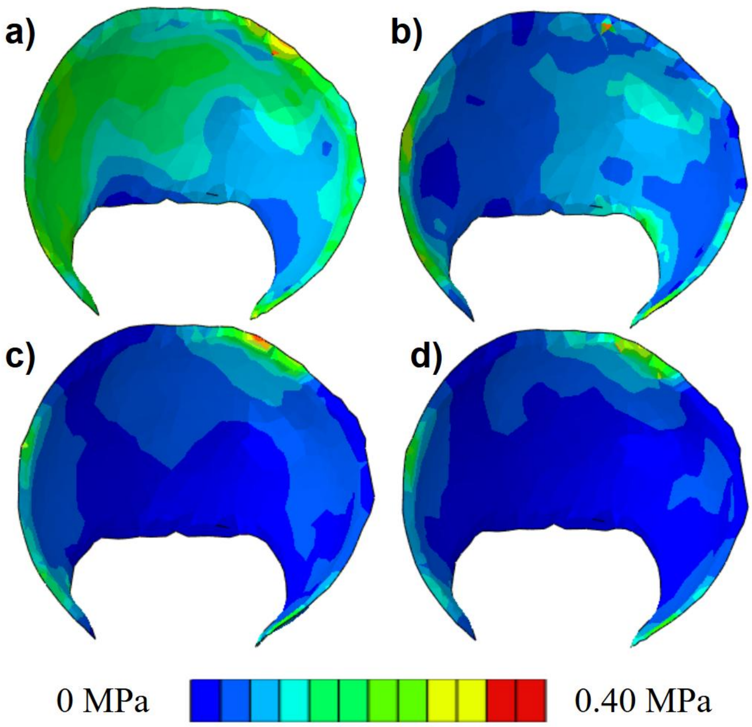

Figure 8.2: The load distribution of the maximum principal strain in the acetabular cartilage during walking stance at a) the initial heel strike (1 % if stance phase) b) the first peak of the ground reaction force (10 % of the stance phase), c) the second peak in the ground reaction force (44 % of the stance phase) and d) mid-stance (50 % of the stance phase).